

MASTER SCIENCE DE LA MATIÈRE
Ecole Normale Supérieure de Lyon
Université Claude Bernard Lyon I



2025 Internship
Romain Ratajczyk
M1 Physique

Study of vortices in XY magnets on the triangular lattice via classical Monte Carlo simulations

This work investigates the XY model on the triangular lattice with interactions up to third neighbors, using classical Monte Carlo simulations. Geometric frustration induces a variety of complex magnetic phases, motivating the implementation of a robust protocol combining optimal gradual cooling and enhanced thermalization techniques. This approach enabled the precise identification of two key transitions: the topological Berezinskii-Kosterlitz-Thouless (BKT) transition—detected via the helicity modulus—and the spontaneous rotational symmetry breaking $C_6 \rightarrow C_2$, characterized through the order parameter \mathcal{O}_6 and the structure factor. We estimated the critical BKT temperature in the thermodynamic limit as $T_{\text{BKT}}^\infty \approx 1.42772$. Along the frustration line $J_3 = J_2/2$, we resolved the continuous transition from the spiral spin liquid to the nematic spiral phase, and mapped the region of broken rotational symmetry in the (J_2, T) phase diagram. In real space, we observed spin vortices and patterns strongly reminiscent of momentum vortices, an open question for the triangular XY model. Although these are well established on the square lattice, our results provide strong numerical evidence for their possible existence in triangular geometry.

Triangular lattice, XY model, Monte Carlo, phase transition, vortices

Supervised by:

Cecilie Glittum

cecilie.glittum@helmholtz-berlin.de

Hahn-Meitner Platz 1, 14109 Berlin, Germany

<https://www.helmholtz-berlin.de>



Contents

Acknowledgements	iii
Introduction	1
1 Theoretical Background and Physical Model	1
1.1 The XY model on the triangular lattice	1
1.2 First approach: the ferromagnetic case with the Berezinskii-Kosterlitz-Thouless (BKT) phase transition	2
1.3 Magnetic phases and frustration	4
1.4 First use of reciprocal space: the energy landscape at $T = 0$ and finite temperature	4
1.4.1 Energy landscape at $T = 0$ compared to finite temperature	4
1.4.2 Fourier transform of the Hamiltonian and momentum space coupling function at $T > 0$. .	5
1.5 $\mathcal{C}_6 \rightarrow \mathcal{C}_2$ Symmetry breaking phase transition along the line $J_3 = J_2/2$	6
1.6 Exotic phases and use of the structure factor	7
2 Numerical Methods and Code Description	8
2.1 Thermal fluctuations activation and need for Monte Carlo	8
2.2 Sampling true equilibrium using Metropolis algorithm and over-relaxation steps	8
2.2.1 Metropolis moves	8
2.2.2 Over-relaxation steps	9
2.2.3 A single step in a flowchart	9
2.3 The warmup phase in details	10
2.3.1 Markov chains and convergence towards the Boltzmann ensemble during warmup phase . .	10
2.3.2 Cooling protocol during warmup phase	11
2.4 Computation of main observables	13
2.4.1 Energy, magnetization and their fluctuations	14
2.4.2 Helicity modulus	14
2.4.3 Structure factor	15
2.4.4 Order parameter \mathcal{O}_6	15
2.5 Complexity and performance considerations	15
3 Results and Discussion	15
3.1 Cooling protocol and warmup phase efficiency	15
3.1.1 Dynamic adjustment of acceptance ratio and sector angle	15
3.1.2 Successive configurations during cooling	17
3.1.3 Conclusion on the warmup phase	19
3.2 Berezinskii-Kosterlitz-Thouless phase transition for various lattice sizes	19
3.2.1 Large scan in temperature of main observables	20
3.2.2 Looking for unbinding of vortex-antivortex pairs in real space	20
3.2.3 Estimated value for transition temperature in the thermodynamic limit	20
3.3 Localization of lattice rotational symmetry-breaking $\mathcal{C}_6 \rightarrow \mathcal{C}_2$	22
3.3.1 Characterization of the nematic spiral phase with a heatmap of the \mathcal{O}_6 order parameter .	22
3.3.2 Looking for momentum vortices in real space	23
Conclusion	23
Appendix A	23
Appendix B	27
Appendix C	28

Acknowledgements

I would like to thank Johannes for welcoming me into his team and for giving me the opportunity to work on a challenging but very interesting topic, both numerically and physically. I've learned a lot from this experience. I'm also very grateful to Cecilie for her support throughout the internship, and for her many helpful suggestions and feedback on my report — it really helped me.

Finally, many thanks for giving me access to the Freie Universität HPC cluster [1], without which I wouldn't have been able to run such large-scale simulations. Finally, thank you to Matías, Tim, and the whole team for their kindness and for making me feel welcome.

Introduction

Vortices are topological excitations central to two-dimensional magnetism. Kosterlitz and Thouless showed in the 1970s how spin vortices stabilize in the 2D XY model, leading to a topological phase transition. Decades later, Yan and Reuther found that frustration can produce a different kind of vortex: in a square-lattice XY model with competing interactions, momentum vectors of spin spirals can form vortex-like textures. This occurs when the energy landscape develops a ring-like minimum in momentum space—a feature also present on the triangular lattice. Whether momentum vortices are stabilized in this geometry, however, remains unresolved. This is why the triangular lattice is very interesting, in addition to its rich variety of phases induced by its intrinsic geometric frustration.

In this work, we focus on two key transitions: the *Berezinskii-Kosterlitz-Thouless* (BKT) transition, topological in nature, and the $C_6 \rightarrow C_2$ transition, involving spontaneous breaking of the triangular lattice's spin rotational symmetry.

We use classical Monte Carlo simulations to mimic thermal fluctuations and perform time-averaged measurements on systems up to size $L = 200$. Particular attention is dedicated to the thermalization phase, ensuring convergence to Boltzmann equilibrium.

Our objective is to precisely detect the BKT transition, explore how frustration shapes the phase diagram of rotational symmetry breaking, with particular attention to the emergence of nematic and spin liquid behavior, and to investigate the presence of spin and momentum vortices in real space.

1 Theoretical Background and Physical Model

1.1 The XY model on the triangular lattice

A classical XY spin is a unit vector in the XY plane, represented as $\vec{S}_i = (\cos \phi_i, \sin \phi_i)$ on site i , where $\phi_i \in [0, 2\pi)$. We consider three possible interactions: between nearest neighbors, next-nearest neighbors, and third neighbors. The Hamiltonian is then given by:

$$\mathcal{H} = J_1 \sum_{\langle i,j \rangle_1} \vec{S}_i \cdot \vec{S}_j + J_2 \sum_{\langle i,j \rangle_2} \vec{S}_i \cdot \vec{S}_j + J_3 \sum_{\langle i,j \rangle_3} \vec{S}_i \cdot \vec{S}_j, \quad (1)$$

where the sums run over the nearest neighbors ($\langle i,j \rangle_1$), second nearest neighbors ($\langle i,j \rangle_2$), and third nearest neighbors ($\langle i,j \rangle_3$) of the spin \vec{S}_i . J_1, J_2, J_3 are the exchange couplings for first, second, and third nearest neighbors respectively. With this convention of the Hamiltonian, we immediately see that a negative coupling constant $J < 0$ characterizes a ferromagnetic interaction. Throughout this report, we set $|J_1| = 1$ and $k_B = 1$, so that energy is measured in units of $|J_1|$ and temperature in units of $|J_1|/k_B$. The triangular lattice is characterized by its basis vectors:

$$\vec{a}_1 = (1, 0), \quad \vec{a}_2 = \left(\frac{1}{2}, \frac{\sqrt{3}}{2} \right),$$

where the lattice spacing a is set to unity. The triangular lattice structure is shown in Figure 1 where we also show the relevant neighbours of a given site.

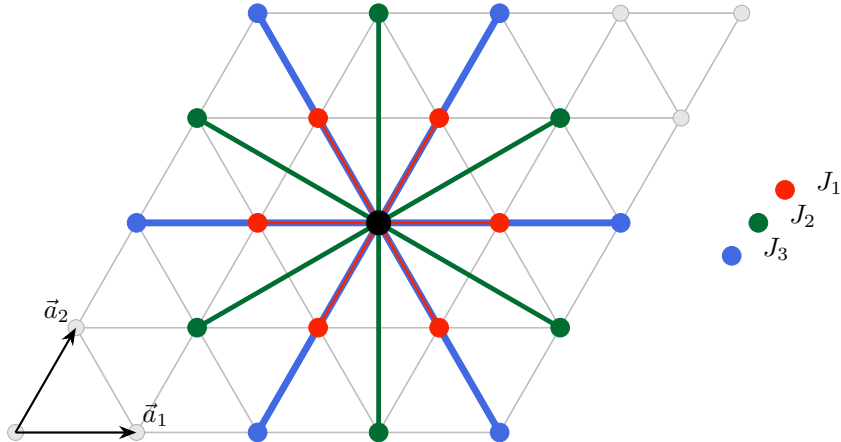


Figure 1: Triangular lattice with up to third-nearest-neighbor exchange interactions shown in orange, green, and blue respectively, emanating from an arbitrary site (black). The basis vectors \vec{a}_1 and \vec{a}_2 are shown as black arrows. Legend: J_1 (nearest neighbors, distance a), J_2 (next-nearest neighbors, distance $\sqrt{3} a$), J_3 (third neighbors, distance $2a$).

We can easily imagine that the intensity of the interactions decreases with distance, so that $|J_1| > |J_2| > |J_3|$. The relative values of these parameters control the richness of possible magnetic configurations in the system. To begin, let us focus on the purely ferromagnetic case, with only $J_1 = -1.0$ and $J_2 = J_3 = 0.0$. This is the simplest case, but it already shows a very interesting phase transition: the **Berezinskii-Kosterlitz-Thouless** (BKT) transition, which is the subject of the next section.

1.2 First approach: the ferromagnetic case with the Berezinskii-Kosterlitz-Thouless (BKT) phase transition

Unlike conventional phase transitions, which involve spontaneous symmetry breaking and the appearance of a local order parameter, the BKT transition is a **topological** phase transition. It is characterized by a change in the behavior of topological defects in the system, called vortices, which are specific high- T configurations of the spins. But at low temperature, the spins will tend to all align in the purely ferromagnetic case, leading to patterns like the one shown in Figure 2:



Figure 2: All spins are aligned, minimizing the energy. This is the favored configuration at very low temperature in the purely ferromagnetic case. Figure from [2].

It is only at high temperature that the spins can form vortices. A vortex in the XY model is defined by the winding number of the spin angle θ around a closed loop:

$$n = \frac{1}{2\pi} \oint_C d\theta,$$

where n is a topological integer. For a single vortex, the angle θ increases by $2\pi n$ when C encloses the vortex core.

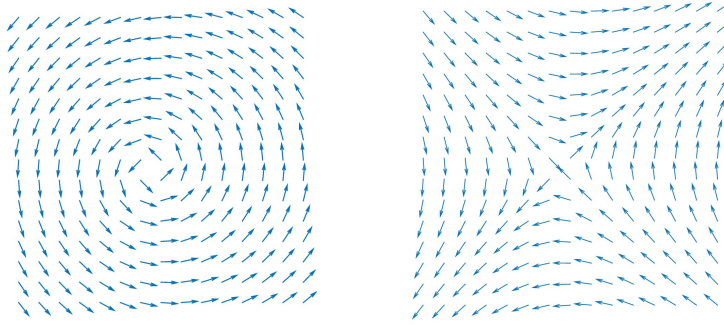


Figure 3: Ideal examples of a vortex ($n = +1$, left) and an antivortex ($n = -1$, right) for the XY spin model $\vec{S}_i = (\cos(\phi(\vec{r}_i)), \sin(\phi(\vec{r}_i)))$. Each image shows the spin configuration in real space, with arrows representing the local spin directions. Figures from [2].

The energy of an isolated vortex in a 2D system diverges logarithmically with the system size L in thermodynamic limit:

$$E_{\text{vortex}} \sim \pi J n^2 \ln \left(\frac{L}{a} \right),$$

where J is the ferromagnetic coupling constant between nearest neighbors [3]. The discoverers of the BKT transition noticed that a vortex-antivortex pair costs much less energy than an isolated vortex, as illustrated in Figure 4:

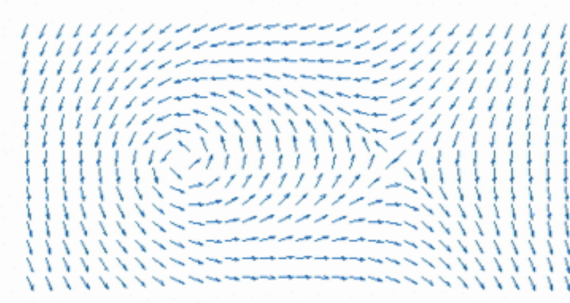


Figure 4: A free isolated vortex is expansive in energy, so that at low temperature, vortices (right, $n = +1$) and anti-vortices (left, $n = -1$) form tightly bound pairs, minimizing their energy, and it costs a lot in energy to unbind them. Figure from [2].

As temperature increases, entropy through thermal fluctuations can suddenly unbind these pairs. The proliferation of free vortices begins at the transition temperature T_{BKT} , destroying quasi-long-range order and make the rigidity of the system collapsing. A useful observable to detect the transition is the helicity modulus Υ . The helicity modulus is the second derivative of the Helmholtz free energy:

$$\Upsilon = \left. \frac{\partial^2 \mathcal{F}(\alpha)}{\partial \alpha^2} \right|_{\alpha=0},$$

and its exact computation formula will be detailed in the numerical section. It describes how rigid the system is against a twist of angle α . The system suddenly loses its rigidity when the vortices unbind at T_{BKT}^+ and Υ naturally vanishes as the rigid structure of the system is destroyed. It is important to understand that a twist means a spatially dependent change of the spin angles, i.e., $\phi_i \rightarrow \phi_i + \alpha \frac{x_i}{L}$, and does not refer to a global rotation of all spins by the same angle α (i.e., $\phi_i \rightarrow \phi_i + \alpha$ for all i), which is an exact symmetry of the Hamiltonian (the global U(1) spin-rotation symmetry) that cannot be broken at finite temperature $T > 0$ in our 2D continuous XY model by the Mermin-Wagner theorem [4].

The theory predicts a universal jump in the thermodynamic limit ($L \rightarrow \infty$) in the helicity modulus as a signature of the BKT transition:

- Universal jump in the helicity modulus Υ at T_{BKT} (see [5]):

$$\Upsilon(T_{BKT}^-) = \frac{2}{\pi} T_{BKT}, \quad \Upsilon(T_{BKT}^+) = 0,$$

- Change in the decay of correlations: Below T_{BKT} , correlations decay as a power law; above T_{BKT} , they decay exponentially [5].

Specific heat and magnetic susceptibility can also indicate a phase transition, but in the case of the BKT transition, they are less precise than the helicity modulus Υ , as we will see in section 3.

1.3 Magnetic phases and frustration

Let us now consider instead the purely antiferromagnetic case ($J_1 > 0$, $J_2 = J_3 = 0$). This introduces the concept of **geometric frustration** and makes the situation more complex. Frustration is the inability to simultaneously minimise all terms of the Hamiltonian. It is not possible in our case for geometrical purpose. The simplest example of a frustrated system is a single triangle with antiferromagnetic interactions, as illustrated in Figure 5. This follows from the fact that three spins cannot be simultaneously antiparallel. Instead, for the XY model, the total energy of the triangle is minimised by the so-called 120 degree order, where the three spins all form 120 degrees with one another. This is a compromise, as no bond is satisfied, however no bond is completely unsatisfied either.

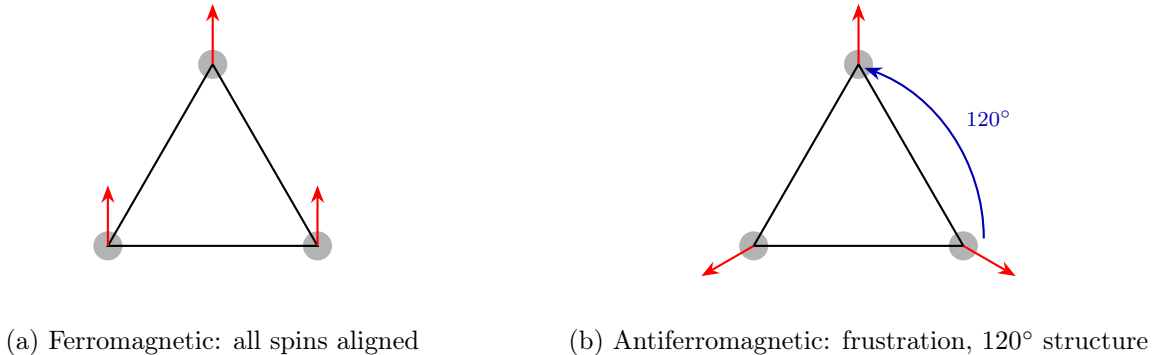


Figure 5: Illustration of geometric (or magnetic) frustration on a triangular elementary cell. (a) Ferromagnetic case: all spins can align (here, all up). (b) Antiferromagnetic case: spins cannot all be antiparallel, leading to a 120° structure (frustration).

For a purely antiferromagnetic system, there are already two possible configurations for a single elementary cell (the one illustrated in Figure 5 (b), and the same but with the spins aiming at the center). When the configuration on a single cell is given, the remaining triangular lattice follows automatically. This is an example of how frustrated magnets often order in so-called spiral states:

$$\vec{S}(\vec{r}) = (\cos(\vec{q} \cdot \vec{r}), \sin(\vec{q} \cdot \vec{r})), \quad (2)$$

where \vec{q} is the spiral ordering wave vector. In the case of the 120° state, $\vec{q} = \pm(4\pi/3, 0)$. When introducing further-neighbor couplings, \vec{q} may become incommensurate or there might be a degeneracy with several \vec{q} 's minimizing the energy. This is what gives rise to the richness and complexity introduced by frustration. And this motivates the use of the reciprocal space, or momentum space, to study the system.

1.4 First use of reciprocal space: the energy landscape at $T = 0$ and finite temperature

To study our system, we will often use the reciprocal lattice, or momentum space, where the wavevectors \vec{q} live. Let us start by presenting the energy landscape at $T = 0$.

1.4.1 Energy landscape at $T = 0$ compared to finite temperature

At $T = 0$, the system reaches its ground state with minimal energy. As we saw in the previous subsection, a natural candidate for the minimal energy configuration is when all spins share a common wavevector in

momentum space. This is why, at $T = 0$, we propose the ansatz for all i :

$$\phi_i = \vec{q} \cdot \vec{r}_i.$$

With this ansatz, the Hamiltonian becomes:

$$\mathcal{H} = \sum_{i,j} J_{ij} \cos(\phi_i - \phi_j) = - \sum_{i,j} J_{ij} \cos[\vec{q} \cdot (\vec{r}_i - \vec{r}_j)].$$

This expression can be simplified into a single sum by introducing the neighbors displacement $\vec{\delta} = \vec{r}_i - \vec{r}_j$, then the energy at $T = 0$ becomes:

$$E(\vec{q}) = \sum_{\vec{\delta}} J(\vec{\delta}) \cos(\vec{q} \cdot \vec{\delta}),$$

which live in the momentum space and closely looks like a Fourier transform of the Hamiltonian. The sum runs over all neighbor displacements $\vec{\delta}$, and $J(\vec{\delta})$ takes the value J_1 , J_2 , or J_3 depending on the distance of the coupling characterized by $\vec{\delta}$. We can then map the corresponding energy $E(\vec{q})$ in three dimensions to have a first look at the energy landscape of the system.

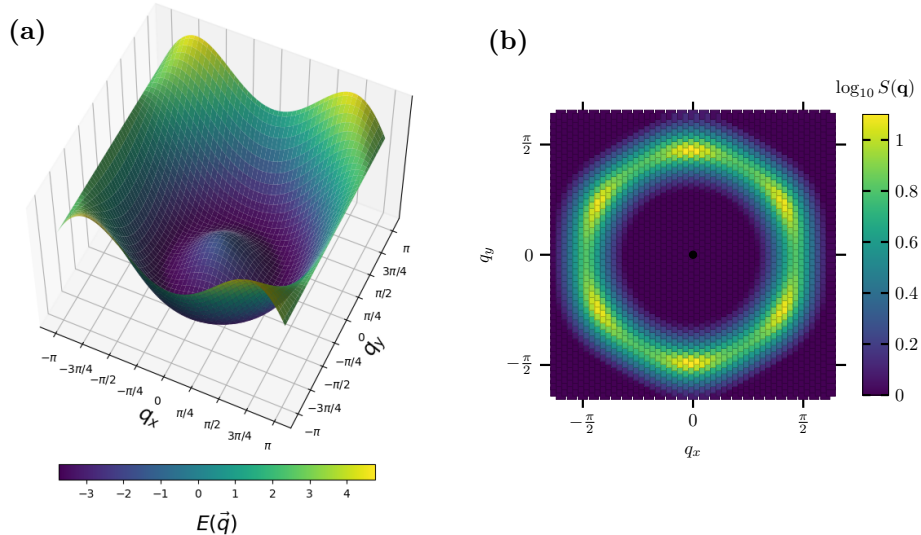


Figure 6: (a) Energy landscape $E(\vec{q})$ in momentum space for $J_1 = -1.0$, $J_2 = 0.5$, $J_3 = 0.25$. (b) Structure factor at $T = 0.48$, showing the wave vectors explored near true equilibrium and forming a hexagonal ring in momentum space.

At $T = 0$, thermal fluctuations are absent and the system settles into a global minimum, selecting a single wavevector q among all those lying on the dark energy ring in 6 (a) (pure "spiral state"). In contrast, at finite temperature ($T > 0$), the system can locally explore a continuum of configurations around the minima of $E(\vec{q})$, which form a hexagonal ring in momentum space (see Figure 6 (b)). The extent of this exploration depends on temperature and the strength of thermal fluctuations. The Helmholtz free energy $\mathcal{F} = E - T\mathcal{S}$ illustrates how entropy can favor slightly higher-energy states as temperature increases. Notably, Figure 6 (b) shows the structure factor at $T = 0.48$ that reveals the restoration of six-fold rotational symmetry, which is broken at very low temperatures. These aspects will be discussed in detail later.

1.4.2 Fourier transform of the Hamiltonian and momentum space coupling function at $T > 0$

Now look at the Hamiltonian at finite temperature $T > 0$. Let us process a Fourier transform of the spins, writing each spin as $\vec{S}_i = \frac{1}{\sqrt{N}} \sum_{\vec{q}} \vec{S}_{\vec{q}} e^{i\vec{q} \cdot \vec{r}_i}$. Inserting this expression into the Hamiltonian (see equation 1) and using standard manipulations (detailed in appendix 3.3.2), one obtains

$$\mathcal{H} = \sum_{\vec{q}} J(\vec{q}) \left| \vec{S}_{\vec{q}} \right|^2,$$

where the *momentum space coupling function* is given by $J(\vec{q}) = \sum_{\vec{\delta}} J(\vec{\delta}) e^{i\vec{q} \cdot \vec{\delta}}$.

Therefore, the Hamiltonian is diagonal in momentum space, and minimizing the energy reduces to finding the minima of $J(\vec{q})$. This analysis has been carried out in [6] and is summarized in Figure 7:

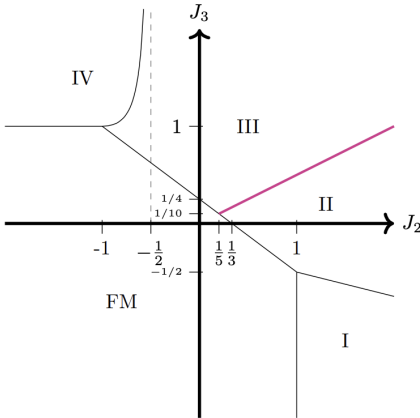


Figure 7: Regions of different classes of wave vectors \vec{q} minimizing $J_{\vec{q}}$ for ferromagnetic (FM) nearest neighbour coupling, $J_1 = -1$.

Remarkably, Figure 7 shows that on the special line $J_3 = J_2/2$, the set of minimizing wavevectors forms a continuous manifold instead of a discrete set. Such a continuous degeneracy is a necessary condition for the emergence of a *Spiral Spin Liquid* (SSL)[6], as discussed in the next section.

These different regions are exceptionally rich in physical phenomena—much more than could be fully explored in a three-month internship. We will therefore focus our investigation on this line $J_3 = J_2/2$. Figure 6 (b) provides an example of the SSL phase just above the transition temperature: at higher T , the intensity along the ring becomes more uniform. The Spiral Spin Liquid (SSL) is the high-temperature phase, appearing just above the transition, where the structure factor $S(\vec{q})$ displays a continuous ring and all lattice symmetries are preserved. At lower temperatures, the system undergoes a symmetry breaking, selecting specific wave vectors and reducing the rotational symmetry from C_6 to C_2 as we will discuss now.

1.5 $C_6 \rightarrow C_2$ Symmetry breaking phase transition along the line $J_3 = J_2/2$

The triangular lattice possesses a six-fold rotational symmetry described by the cyclic group C_6 , generated by successive 60° rotations around a lattice site. Each site has six nearest neighbors along directions separated by 60° , which are $\vec{a}_1, \vec{a}_2, \vec{a}_3 = -\vec{a}_1 + \vec{a}_2$, and their opposites. At high temperature, these directions are statistically equivalent due to thermal fluctuations. However, at low temperature, the system tends to favor particular orientations, breaking the C_6 symmetry group down to C_2 subgroup (invariance under 180° rotations only). The system also loses the long-range order above the transition at high temperatures. (long-range order is forbidden by the Mermin-Wagner theorem in 2D at finite temperature, but it can be observed because of finite-size effects). This spontaneous symmetry breaking is captured by the complex order parameter \mathcal{O}_6 , defined as (see [7]):

$$\mathcal{O}_6 = \frac{1}{2N} \sum_{\vec{R}} \left\langle \cos(\theta_{\vec{R}} - \theta_{\vec{R}+\vec{a}_1}) + \omega \cos(\theta_{\vec{R}} - \theta_{\vec{R}+\vec{a}_2}) + \omega^2 \cos(\theta_{\vec{R}} - \theta_{\vec{R}+\vec{a}_3}) \right\rangle. \quad (3)$$

The angles $\theta_{\vec{R}}$ are the spin angles at site \vec{R} , and \vec{a}_1, \vec{a}_2 , and \vec{a}_3 are the three nearest-neighbor directions in the triangular lattice. The primitive third root of unity ω , satisfying $1 + \omega + \omega^2 = 0$, provides an elegant algebraic tool to weight contributions from the three nearest-neighbor directions such that when the spin differences along these directions are statistically equivalent (as above the transition temperature), their weighted sum cancels exactly, making the order parameter \mathcal{O}_6 vanish.

Above the transition, where no orientation is favored, it is natural to wonder whether momentum vortices and anti-vortices might appear in real space. This phenomenon is well established for the XY model on the square lattice (see [8]), where a similar ring minimum in $E(\vec{q})$ exists, but its presence in the triangular XY model remains to be clarified. In the following Figure 8, we illustrate the momentum vortices and anti-vortices as they appear in the square lattice:

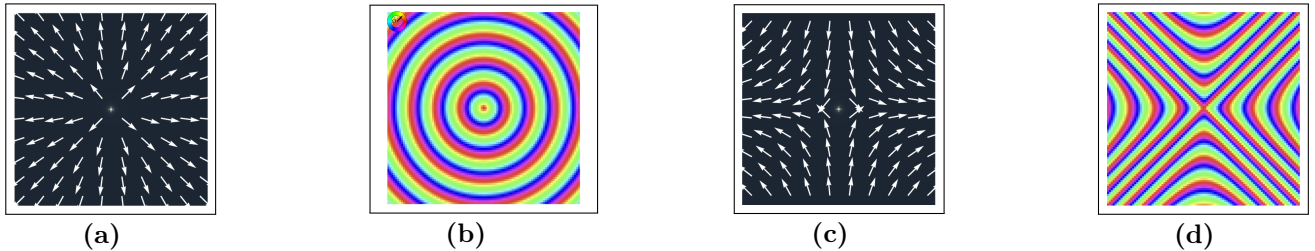


Figure 8: (a) Example of an ideal momentum vortex in momentum space, (b) the corresponding momentum vortex in real space. (c) Example of an ideal momentum anti-vortex in momentum space, (d) the corresponding ideal momentum anti-vortex in real space. Momentum is $\vec{\nabla}\phi(\vec{r})$ where $\phi(\vec{r})$ is the spin orientation, and all four pictures concern the square geometry. We will discuss the presence of this momentum vortices in the triangular lattice in section 3.3.1. Figures adapted from [8].

The construction of \mathcal{O}_6 captures the breaking of six-fold rotational symmetry below the critical temperature, which is also the transition between two important magnetic phases: the *spiral phase* and the *spiral spin liquid* (SSL) phase.

1.6 Exotic phases and use of the structure factor

As we have already begun to see, the triangular lattice with further-neighbour couplings J_2, J_3 is very rich and supports a variety of exotic magnetic phases. These phases are distinguished by the specific patterns with which they break the discrete six-fold lattice-rotation symmetry \mathcal{C}_6 (invariance under rotations by multiples of 60°) down to its two-fold subgroup \mathcal{C}_2 (only 0° and 180° rotations). This discrete symmetry breaking can be detected thanks to the order parameter \mathcal{O}_6 , and is allowed at finite T even in two dimensions, whereas the continuous global U(1) spin-rotation symmetry (rotate all spins by any angle α) cannot be broken at $T > 0$ by the Mermin–Wagner theorem (it may look broken at very low T , but it's a finite size effect).

The key diagnostic for all of these phases is the **structure factor**, which we have already first seen in Figure 6 (b). It is defined as an *ensemble average* in the Boltzmann distribution (see [9]):

$$S(\vec{q}) = \frac{1}{N} \left\langle \sum_{i,j} \vec{S}_i \cdot \vec{S}_j e^{i\vec{q} \cdot (\vec{r}_j - \vec{r}_i)} \right\rangle, \quad (4)$$

and it points in momentum space where correlations are strongest (its detailed computation will appear in the numerical section). Equivalently, since $\vec{S}_i \cdot \vec{S}_j = \cos(\phi_i - \phi_j)$, $S(\vec{q})$ can be seen as the Fourier transform of a cosine correlation. If the system selects only a single wave vector \vec{q}_0 (which typically happens at $T = 0$ or at very low T), it results in two symmetric Dirac peaks at $\pm\vec{q}_0$ in reciprocal space. At finite temperature $T > 0$, if several wave vectors are favored, the complex exponentials in the structure factor will add coherently for each of these \vec{q} values. This leads to multiple quasi-Dirac peaks in $S(\vec{q})$, each less intense than in the perfectly ordered case.

As temperature increases along the line $J_3 = J_2/2$, one typically encounters in order:

- **Spiral-ordered phases**, in which a single wavevector \mathbf{q}_0 is frozen from the degenerate ring, resulting in two symmetric Dirac peaks in $S(\mathbf{q})$ at $\pm\vec{q}_0$, again breaking $\mathcal{C}_6 \rightarrow \mathcal{C}_2$ but preserving a combined spin-rotation–translation invariance ($\mathcal{O}_6 > 0$). This typically occurs at $T = 0$, where the U(1) spin-rotation symmetry is spontaneously broken (this does not contradict the Mermin–Wagner theorem, which concerns $T > 0$) but can also be observed at very low $T > 0$.
- **Nematic spiral liquids**, at intermediate T , where the chosen \mathbf{q}_0 spreads into an arc on the ring, reflecting the selection of a particular ordering wave vector—nematic order ($\mathcal{C}_2, \mathcal{O}_6 > 0$) remains but the Bragg peak in $S(\mathbf{q})$ broadens [6].
- **Spiral-disordered phases**, in which several wavevectors \mathbf{q} on the degenerate ring are explored (a discrete collection of wave-vectors). The \mathcal{C}_6 symmetry is partially restored, but nematic order ($\mathcal{O}_6 > 0$) remains as the ring in momentum space is not fully explored.
- **Spiral spin liquid (SSL)**, where full and continuous exploration of the degenerate ring restores \mathcal{C}_6 ($\mathcal{O}_6 = 0$) yet maintains strong local spiral correlations, yielding a diffuse hexagonal pattern in $S(\mathbf{q})$. The continuous ring in \vec{q} -space indicates that the system lacks a unique ordering direction. This is where we expect momentum vortices [8].

- **Paramagnetic phase**, at high T , in which all correlations are short-ranged and both $U(1)$ and \mathcal{C}_6 symmetries are fully restored ($\mathcal{O}_6 = 0$). One observes a diffuse peak at the center of the first Brillouin zone for $S(\mathbf{q})$, without any particular geometry elsewhere, which shows the absence of long-range correlations.

The structure factor is a very powerful tool to explore the properties of the different phases in our system. It allows us to identify the type of magnetic order present by analyzing the location and shape of the peaks of $S(\vec{q})$ in reciprocal space.

2 Numerical Methods and Code Description

2.1 Thermal fluctuations activation and need for Monte Carlo

Thermal fluctuations

At a finite temperature $T > 0$, the system tries to minimize its free energy $\mathcal{F} = E - TS$, where S is the entropy. The system can then explore the energy landscape near the true equilibrium, as the activation of thermal fluctuations allows the system to hop over energy barriers of order $k_B T$, where k_B is the Boltzmann constant.

Why Monte Carlo is natural in this context

Fundamentally, the Monte Carlo method is the explicit use of random variables in a stochastic process (that is, a random process evolving over time). In our case, the main goal is to accumulate observables **at fixed temperature** by sampling equilibrium configurations, which the system explores thanks to thermal fluctuations. In other words, we perform a time average along a stochastic trajectory in phase space (a trajectory statistically confined near physical equilibrium). This makes the Monte Carlo method a natural choice for our simulations.

2.2 Sampling true equilibrium using Metropolis algorithm and over-relaxation steps

The phase in which we accumulate observables is called the **measurement phase**, and it takes place **at fixed temperature**. To simulate thermal fluctuations, we use the Metropolis algorithm. We call a **Metropolis move** the application of this algorithm to a single spin.

2.2.1 Metropolis moves

The Metropolis algorithm is used to explore the energy landscape of the system by proposing random spin flips and accepting or rejecting them based on the change in energy. They simulate thermal fluctuations. At each step, a random spin \vec{S}_i is selected, and a new spin orientation \vec{S}'_i is proposed according to a sector-based Gaussian algorithm: the new suggested angle verify $\phi_{\text{new}} = \phi_{\text{old}} + \mathcal{N}(0, \sigma)$ where $\mathcal{N}(0, \sigma)$ is a Gaussian distribution with mean 0 and standard deviation σ . A schematic representation is shown in Figure 9. Determining σ for each temperature is the objective of the warm-up phase, which occurs before the measurement phase. This will be discussed below. The local change in energy ΔE is calculated as:

$$\Delta E = J_1 \sum_{\langle i,j \rangle_1} (\vec{S}'_i \cdot \vec{S}_j - \vec{S}_i \cdot \vec{S}_j) + J_2 \sum_{\langle i,j \rangle_2} (\vec{S}'_i \cdot \vec{S}_j - \vec{S}_i \cdot \vec{S}_j) + J_3 \sum_{\langle i,j \rangle_3} (\vec{S}'_i \cdot \vec{S}_j - \vec{S}_i \cdot \vec{S}_j), \quad (5)$$

The change in energy ΔE quantifies how much the proposed spin flip alters the system's energy. If $\Delta E < 0$, the new spin orientation is accepted. If $\Delta E \geq 0$, the new orientation is accepted with a probability given by the Boltzmann factor:

$$\mathbb{P}(\Delta E) = \min \left(1, e^{-\Delta E / k_B T} \right), \quad (6)$$

where k_B is the Boltzmann constant and T is the temperature. If the proposed move is accepted, the spin orientation is updated to \vec{S}'_i ; otherwise, it remains unchanged. If the move is accepted the energy is increased by ΔE to avoid global computation of energy, which is very costly in computation time for large systems.

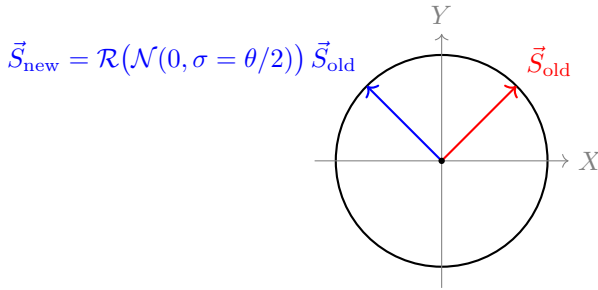


Figure 9: Illustration of the suggestion of a Metropolis move: \mathcal{R} is a rotation matrix; the old spin \vec{S}_{old} is rotated by an angle chosen in a Gaussian width to obtain the new spin \vec{S}_{new} . The Gaussian width (more precisely the angle θ) is adapted before the measure phase to ensure that the acceptance rate is around 50% (see the warmup phase section).

2.2.2 Over-relaxation steps

Over-relaxation steps are used to further explore the energy landscape and reduce correlations between successive configurations [9]. In this step, a random spin \vec{S}_i is selected, and its orientation is reflected with respect to the local effective field generated by its neighbors. The local effective field at site i is defined as:

$$\vec{H}_{\text{eff}} = \sum_j J_{ij} \vec{S}_j.$$

The over-relaxation move consists in reflecting the spin \vec{S}_i with respect to \vec{H}_{eff} :

$$\vec{S}'_i = -\vec{S}_i + 2 \frac{\vec{S}_i \cdot \vec{H}_{\text{eff}}}{\|\vec{H}_{\text{eff}}\|^2} \vec{H}_{\text{eff}},$$

We can check that this transformation leaves the energy unchanged:

$$\vec{S}'_i \cdot \vec{H}_{\text{eff}} = \left(-\vec{S}_i + 2 \frac{\vec{S}_i \cdot \vec{H}_{\text{eff}}}{\|\vec{H}_{\text{eff}}\|^2} \vec{H}_{\text{eff}} \right) \cdot \vec{H}_{\text{eff}} = -\vec{S}_i \cdot \vec{H}_{\text{eff}} + 2 \frac{\vec{S}_i \cdot \vec{H}_{\text{eff}}}{\|\vec{H}_{\text{eff}}\|^2} \|\vec{H}_{\text{eff}}\|^2 = -\vec{S}_i \cdot \vec{H}_{\text{eff}} + 2\vec{S}_i \cdot \vec{H}_{\text{eff}} = \vec{S}_i \cdot \vec{H}_{\text{eff}}.$$

Therefore, the total energy remains unchanged by the over-relaxation move.

Quench steps

Over-relaxation moves are also useful for visualization purposes. If you want to remove thermal fluctuations to display a nice spin configuration, you can sweep through the lattice several times (30 times is more than enough) using only over-relaxation moves. This allows you to "quench" the system, meaning it will converge to a low-energy state where all the spins are locally aligned with the field. This practice is obviously not used for statistics; it is only used on rare occasions to get an ideal spin configuration to illustrate the theory in the report. It is not a physical method because it removes thermal fluctuations.

2.2.3 A single step in a flowchart

Metropolis moves and over-relaxation moves are the two types of updates used at each step in any phase of the simulation. To give a better overview of the method, we show a flowchart of a single Monte Carlo step in Figure 10:

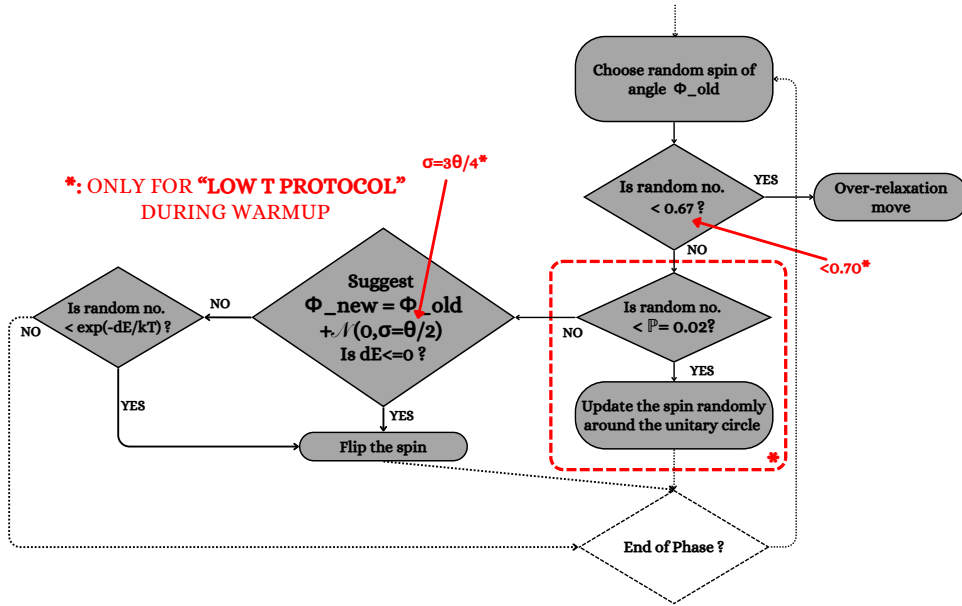


Figure 10: The Core of a Monte Carlo Simulation in a Flowchart. A measurement phase lasts $500\,000 \times L^2$ such steps, where L is the size of the triangular lattice. We accumulate observables at regular intervals, which can't be seen in this chart. In red are details that are present only during the **warmup phase**. This phase comes before the measurement phase and is essential to reach Boltzmann equilibrium, which ensures that we accumulate our observables from configurations representative of physical equilibrium.

2.3 The warmup phase in details

The warmup phase is absolutely crucial to ensure reliable statistics and correct physics in Monte Carlo simulations. I realized the importance of this phase several times during my internship, which led me to continually improve its robustness. In fact, it was by far the most time-consuming part of the code development.

2.3.1 Markov chains and convergence towards the Boltzmann ensemble during warmup phase

The canonical expectation of an observable A is formally defined as

$$\mathbb{E}_T[A] = \frac{1}{Z} \int e^{-\beta \mathcal{H}(x)} A(x) dx.$$

In practice, our Monte Carlo code generates during the measure phase a discrete Markov chain $\{\mathcal{C}\}$ sampling configurations whose canonical distribution is the Boltzmann weight $\mathbb{P}_{\text{eq}}(\mathcal{C} \in \mathcal{C}) = e^{-\beta \mathcal{H}(\mathcal{C})}/Z$. Therefore, the average over M uncorrelated configurations (understand that \mathcal{C}_m and \mathcal{C}_{m+1} are not two consecutive configurations in the Markov chain, but rather two configurations separated by a large number of steps)

$$\hat{A}_M = \frac{1}{M} \sum_{m=1}^M A(\mathcal{C}_m),$$

converges to $\mathbb{E}_T[A]$ as $M \rightarrow \infty$ without explicitly calculating the partition function Z .

But this **assumes that the Boltzmann equilibrium has already been reached**. However, the first step of a simulation is the random initialization of the spins: at this point, we are far from the canonical distribution \mathbb{P}_{eq} . The warmup phase ensures that we reach this equilibrium by building an initial Markov chain $\{\mathcal{C}_k\}_k$ whose required properties are satisfied by our code. Each update $\mathcal{C}_k \rightarrow \mathcal{C}_{k+1}$ (now understand \mathcal{C}_k and \mathcal{C}_{k+1} as two consecutive configurations) is drawn from a transition kernel $W(\mathcal{C}_k \rightarrow \mathcal{C}_{k+1})$ that must satisfy:

1. Detailed balance

$$\mathbb{P}_{\text{eq}}(\mathcal{C}) W(\mathcal{C} \rightarrow \mathcal{C}') = \mathbb{P}_{\text{eq}}(\mathcal{C}') W(\mathcal{C}' \rightarrow \mathcal{C}),$$

with

$$W(\mathcal{C} \rightarrow \mathcal{C}') = q(\mathcal{C} \rightarrow \mathcal{C}') \cdot A(\mathcal{C} \rightarrow \mathcal{C}'),$$

where q is the probability to propose \mathcal{C}' from \mathcal{C} , and A is the acceptance probability.

In our Metropolis algorithm, proposals are made by $\phi_{\text{new}} = \phi_{\text{old}} + \mathcal{N}(0, \sigma)$. The symmetric distribution makes q symmetric, that is, $q(\mathcal{C} \rightarrow \mathcal{C}') = q(\mathcal{C}' \rightarrow \mathcal{C})$. We accept the proposal with $A(\mathcal{C} \rightarrow \mathcal{C}') = \min(1, e^{-\beta \Delta \mathcal{H}})$. This means that

$$\frac{W(\mathcal{C} \rightarrow \mathcal{C}')}{W(\mathcal{C}' \rightarrow \mathcal{C})} = \frac{A(\mathcal{C} \rightarrow \mathcal{C}')}{A(\mathcal{C}' \rightarrow \mathcal{C})} = e^{-\beta \Delta \mathcal{H}},$$

which satisfies detailed balance.

2. Ergodicity, irreducibility, and aperiodicity

These are ensured because our algorithm can, in principle, reach any configuration from any other by a sequence of random moves (ergodicity and irreducibility), and the randomness of the moves prevents the chain from cycling deterministically (aperiodicity).

3. Conclusion

Under these conditions, one can show rigorously that

$$\lim_{k \rightarrow \infty} \mathbb{P}(\mathcal{C}_k) = \mathbb{P}_{\text{eq}}(\mathcal{C}).$$

Our Warmup Markov chain then converges to the equilibrium Boltzmann distribution. We are now ready to continue this Markov chain in what is called the measurement phase (since there is actually a single chain, which reaches equilibrium and stays there). In this phase, we accumulate observables from this equilibrium distribution by calculating them from configurations \mathcal{C} that are sufficiently spaced in the chain to avoid correlations.

2.3.2 Cooling protocol during warmup phase

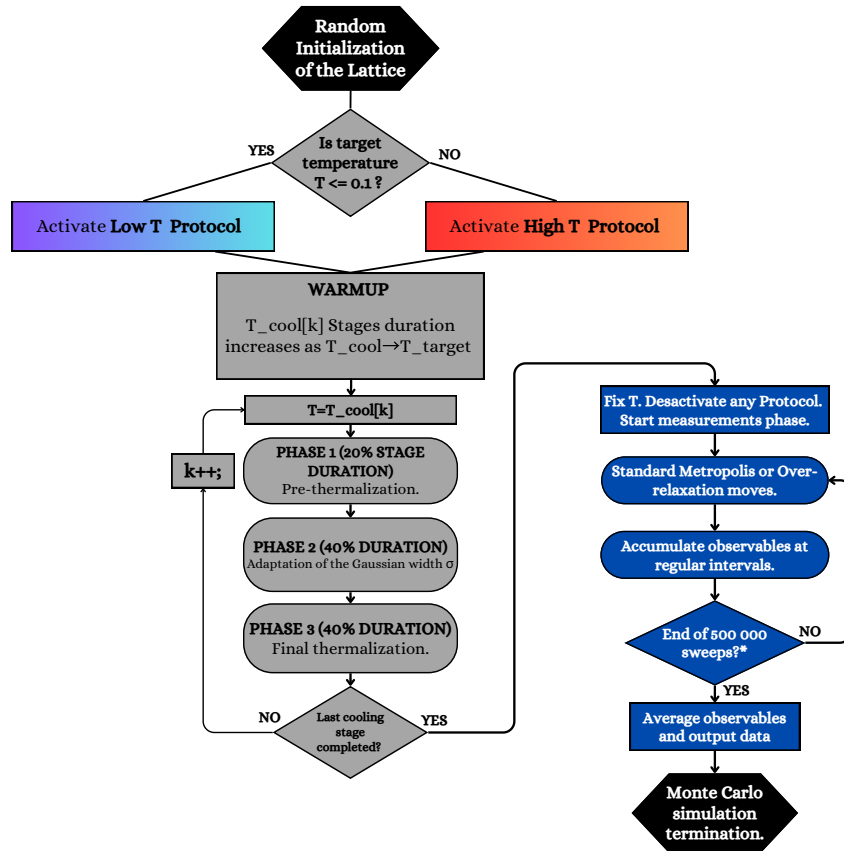


Figure 11: A full Monte Carlo simulation, including the warmup phase that precedes the measurement phase. The warmup phase is crucial to ensure that the system reaches thermal equilibrium before we start accumulating observables. It includes a cooling schedule, where the temperature is gradually lowered down to the measurements target temperature, and is divided into three subphases, each with a specific role detailed below. At each step of each subphase, we basically perform same algorithm as in Figure 10.

- The lattice is initialized with random spins.

- The first condition sets the boundary between "low temperature" and "high temperature" at $T = 0.1$. Below this temperature, thermal fluctuations are less effective (see Results section).
- When the "**High T Protocol**" is active, the cooling schedule uses a polynomial law: $T_{\text{cool}}[k] = T + (T_{\text{start}} - T) \left(1 - \frac{k}{N_{\text{cool}} - 1}\right)^{\alpha}$ for k from 0 to $N_{\text{cool}} - 1 = 7$ (8 cooling steps), with $\alpha = 3$ and $T_{\text{start}} = T + 0.5 = T_{\text{cool}}[0]$.
- When the "**Low T Protocol**" is active, the cooling schedule uses a geometric law: $T_{\text{cool}}[k] = T_{\text{start}} \left(\frac{T}{T_{\text{start}}}\right)^{k/(N_{\text{cool}} - 1)}$ for k from 0 to $N_{\text{cool}} - 1 = 7$ (8 cooling steps), with $T_{\text{start}} = T + 0.5 = T_{\text{cool}}[0]$. Advanced Metropolis techniques are also used: the Gaussian width is increased, the proportion of over-relaxation moves is increased from $2/3$ to 0.70 , and with a small probability (2%), global moves are proposed in $[-\pi, \pi]$. See Figure 12 for a numerical illustration of the proportions of different moves during the warmup phase.
- In both protocols, the total warmup duration at $T_{\text{cool}}[k]$ is a fraction of $333,333 \times L^2$ steps, given by $\text{warmup_fraction}(T_{\text{cool}}[k]) = f_{\text{start}} + (f_{\text{end}} - f_{\text{start}}) \frac{T_{\text{start}} - T_{\text{cool}}[k]}{T_{\text{start}} - T}$, where $f_{\text{start}} = 0.25$ and $f_{\text{end}} = 1.0$. The duration approaches 100% as the cooling temperature gets closer to the target temperature. See Table 1 which illustrates the cooling schedule and the warmup duration for two different target temperatures $T = 1.44$ and $T = 0.0001$.
- **Phase 1** for temperature $T_{\text{cool}}[k]$ lasts 20% of $\text{warmup_fraction}(T_{\text{cool}}[k]) \times 333,333 \times L^2$, and phases 2 and 3 last 40% each.
- Phase 1 is a "pre-thermalization" phase. The algorithm described in Flowchart 1 is used at each step, just like in phases 2 and 3, but phases 2 and 3 have extra features. For phase 1 of the first cooling temperature, the angle θ is set to π , so the Gaussian width for Metropolis moves is $\pi/2$. The acceptance ratio (number of accepted Metropolis moves over proposed moves) is measured regularly (every $100 \times L^2$ moves).
- **Phase 2** is the adaptation phase for the Gaussian width used in Metropolis moves. In addition to the moves described in Flowchart 1, the Gaussian width is updated every $10 \times L^2$ moves. The method is: at each update, take the average of the last 20 acceptance ratios, call it r_{avg} . Also count the number of updates N_{adapt} so far. The angle θ is updated according to the deviation from the target acceptance 0.5: $\theta \leftarrow \theta \times \exp\left(\frac{1}{\sqrt{N_{\text{adapt}}}} \cdot (r_{\text{avg}} - 0.5)\right)$. The adaptation becomes finer as phase 2 progresses, thanks to the $1/\sqrt{N_{\text{adapt}}}$ factor.
- At the end of phase 2, the average of the last 1000 adapted angles θ is taken, and θ is fixed to this value for phase 3 and the measurement phase.
- **Phase 3** consists in the final thermalization at the current cooling temperature $T_{\text{cool}}[k]$. The acceptance ratio is very close to 50.0%, the angle θ is fixed and is no longer adapted, to focus on thermalization. If the "Low T Protocol" is active, the probability \mathbb{P} to propose global moves decreases linearly as phase 3 progresses, since we are more and more confident that equilibrium has been reached and it is less and less necessary to try to escape a possible metastable state (a local but not global minimum).
- When phase 3 at temperature $T_{\text{cool}}[k]$ is finished, we start phase 1 at temperature $T_{\text{cool}}[k + 1]$, or we move to the measurement phase if $k + 1 = N_{\text{cool}}$.
- Energy, current cooling temperature, step number, corresponding phase, acceptance ratio and adapted angle θ are saved regularly during the three phases of each cooling temperature; spin configurations and structure factor are saved at the end of each cooling temperature stage. These data are used to check the efficiency of the warmup phase.
- The measurement phase is done at fixed temperature ($T = T_{\text{cool}}[N_{\text{cool}} - 1]$), and lasts $500\,000 \times L^2$ steps (500,000 sweeps). Standard Metropolis and over-relaxation moves are performed, following the same protocol described in Figure 11 whatever the temperature: the goal is no longer to thermalize or avoid a metastable state. We consider that equilibrium has been reached, and we simply simulate thermal fluctuations in the same way, whatever the temperature regime. Observables are accumulated every $10 \times L^2$ steps, and averaged over the number of times they have been accumulated at the end of the 500,000 sweeps.
- **The simulation is finished.**

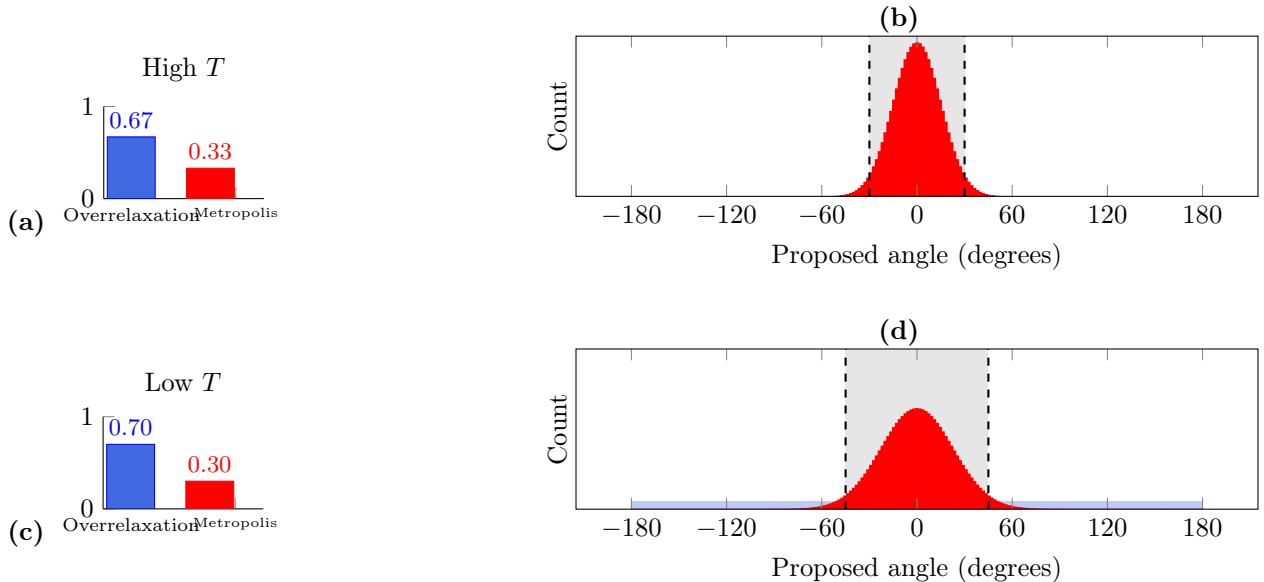


Figure 12: (a) and (c): Proportion of overrelaxation vs Metropolis moves for the two temperature regimes T . (b) and (d): Histogram of Metropolis proposals for the sector-based Gaussian algorithm, both with a sector angle of 30° . (red = standard Metropolis moves, blue = global moves, boosted by 25 for visualization purposes, dashed and gray sector = 95% confidence interval). The chosen angle is arbitrary and in practice strongly depends on the temperature. Keep in mind that the Gaussian is widened at low temperature in the warmup phase to propose a greater variety of moves to try to improve exploration, which is made difficult by the lack of strong enough thermal fluctuations.

Table 1: Cooling schedule and warmup duration (%) for two different target temperatures $T = 1.44$ and $T = 0.0001$. The first triggers a polynomial cooling protocol, the second a geometric cooling protocol. The warmup duration is expressed as a percentage of $333,333 \times L^2$ steps (333,333 Monte Carlo sweeps).

k	$T_{\text{cool}}[k]$ (1.44)	warmup duration (%)	$T_{\text{cool}}[k]$ (0.0001)	warmup duration (%)
0	1.940	25.0	0.5001	25.0
1	1.754	52.9	0.2426	35.7
2	1.622	72.8	0.1177	46.4
3	1.533	86.1	0.0571	57.1
4	1.480	94.0	0.0277	67.9
5	1.452	98.2	0.0134	78.6
6	1.441	99.9	0.0065	89.3
7	1.440	100	0.0001	100

Note: These methods allow for good thermalization and help avoid metastable states as much as possible, although as discussed in section 3, it is never possible to guarantee this completely. In practice, the most effective way to reduce the risk of metastable states is to always start the thermalization from a sufficiently high temperature, where thermal fluctuations are strong. The code ensures this with its cooling protocol, regardless of the target temperature. The advanced Metropolis techniques described above are useful at very low temperatures, but starting from a high temperature remains the key factor for robust thermalization.

2.4 Computation of main observables

In this section, we describe the observables of interest and how we collect them during a simulation. All of the following observables are collected every $10 \times L^2$ steps during the measurement phase, to balance statistical reliability and reduce autocorrelations. We normalize and average them at the end of each simulation.

2.4.1 Energy, magnetization and their fluctuations

Energy and specific heat

The average energy is given by

$$E = \langle \mathcal{H} \rangle,$$

where \mathcal{H} is the Hamiltonian. In practice, we will examine the energy per spin:

$$E_N = \frac{1}{N} E,$$

where $N = L^2$ is the number of spins. As discussed below Eq. (2.2.1), the energy is updated at each step instead of being recalculated from scratch every $10 \times L^2$ steps. This is easy to do with the energy because it changes at each step due to the Metropolis moves, and it saves computation time.

The specific heat, which quantifies energy fluctuations, is by definition: $C_v = \frac{\partial E}{\partial T}$, and we show in appendix 3.3.2 that it can be computed as the fluctuations of the energy:

$$C_v = \frac{\beta^2}{N} (\langle E^2 \rangle - \langle E \rangle^2),$$

where $\beta = 1/k_B T$ is the inverse temperature (we set $k_b = 1$). The specific heat shows peaks or divergences near a phase transition, making it useful for detecting them.

Magnetization and magnetic susceptibility

The magnetization per spin is

$$M = \frac{1}{N} \left\langle \left| \sum_{i=1}^N \vec{S}_i \right| \right\rangle.$$

In our 2D continuous XY model, the magnetization is never a good order parameter. According to the Mermin-Wagner theorem, it vanishes at finite temperature in the thermodynamic limit, even for the purely ferromagnetic case. For a finite-size lattice, a nonzero value can be observed, but at high temperature it scales as $1/\sqrt{N}$ due to the central limit theorem (since spins are nearly independent, see appendix 3.3.2). In the frustrated regime, the magnetization remains close to zero and does not provide useful information. Other observables, such as the specific heat and those described below, are more interesting to study.

The magnetic susceptibility, which measures fluctuations of the magnetization, is by definition $\chi = \frac{\partial M}{\partial H_{\text{eff}}}$ and can be computed as:

$$\chi = \frac{\beta}{N} (\langle |\vec{M}|^2 \rangle - \langle |\vec{M}| \rangle^2).$$

Like the specific heat, the susceptibility is based on fluctuations and can be noisy. It typically exhibits a peak or divergence at a phase transition, including BKT transition. However, we will see in Figure 16 that the helicity modulus is a better observable for detecting this transition.

2.4.2 Helicity modulus

As already elaborated on in section 1.2, it is known that the ferromagnet undergoes a phase transition at a critical temperature T_{BKT} , the so-called **Berezinskii-Kosterlitz-Thouless** (BKT) transition. It is characterized in the thermodynamic limit by a brutal change in the helicity modulus from a finite value below T_{BKT} to zero above it.

The numerical formula for the helicity modulus (helicity stiffness) computed in this code, for the direction $\mu \in \{x, y\}$, is (see [10]):

$$\Upsilon_\mu = \frac{1}{L^2} \left\langle \sum_{\langle i,j \rangle} J_{ij} (\vec{x}_{ij} \cdot \vec{e}_\mu)^2 \cos(\phi_i - \phi_j) \right\rangle - \beta \frac{1}{L^2} \left\langle \left(\sum_{\langle i,j \rangle} J_{ij} (\vec{x}_{ij} \cdot \vec{e}_\mu) \sin(\phi_j - \phi_i) \right)^2 \right\rangle,$$

where:

- J_{ij} is the coupling between sites i and j (J_1, J_2 , or J_3 depending on the neighbor distance),
- \vec{e}_{ij} is the unit vector pointing from site i to site j ,

- \vec{e}_μ is the unit vector in the μ direction (x or y) which do the projection,
- ϕ_i is the angle of the spin at site i ,
- the sum runs over all considered neighbor pairs (first, second, and third neighbors).

The total helicity modulus is the average over both directions:

$$\Upsilon = \frac{\Upsilon_x + \Upsilon_y}{2}.$$

2.4.3 Structure factor

The structure factor $S(\vec{q})$ is defined as the Fourier transform of the correlation function $\vec{S}_i \cdot \vec{S}_j$ (see [9]):

$$S(\vec{q}) = \frac{1}{N} \left\langle \sum_{i,j} \vec{S}_i \cdot \vec{S}_j e^{i\vec{q} \cdot (\vec{r}_j - \vec{r}_i)} \right\rangle, \quad (7)$$

and can be rewritten as a sum of the squared moduli of the Fourier transforms of the spin components (see appendix 3.3.2):

$$S(\vec{q}) = \frac{1}{N} \left\langle |\hat{S}^x(\vec{q})|^2 + |\hat{S}^y(\vec{q})|^2 \right\rangle.$$

We use the module FFTW which compute the two fourier transforms every $10 \times L^2$ steps. Its complexity is $\mathcal{O}(L^2 \log L)$, which save a lot of computational time compared to a direct computation of the structure factor, which would be $\mathcal{O}(L^4)$.

For visualization, it is helpful to remember that the reciprocal lattice is a clockwise rotation of the direct lattice by 30° and is scaled by a factor of $\frac{4\pi}{\sqrt{3}}$ (see 3.3.2 for details).

2.4.4 Order parameter \mathcal{O}_6

We also compute the order parameter \mathcal{O}_6 in the way described in section 1.5.

2.5 Complexity and performance considerations

The complexity of the Monte Carlo simulation is $O(N_T \times L^2 \times \text{MC_Steps})$, where N_T is the number of temperatures, L^2 is the number of spins in the system, and MC_Steps is the number of Monte Carlo steps. This high complexity led me to use a cluster for the simulations. The simulations are parallelized by running each temperature on a separate core. It divides the total run time by N_T .

3 Results and Discussion

3.1 Cooling protocol and warmup phase efficiency

The warmup phase was without a doubt what took me the most time during my internship. It underwent constant revisions, right up to the launch of the main simulations that will be presented here. It is crucial to ensure that we are truly accumulating the real physics of the system during the measurement phase, i.e., that we are in one of the true energy minima, and not in a metastable state. Metastable states must be avoided not only because they do not represent the true state the system would choose if left to evolve long enough, but also because we could end up with artifacts if the system explores the vicinity of such a metastable state during the measurement phase. In the following, we will justify the robustness of the developed warmup protocol and mention the difficulties that can be encountered.

3.1.1 Dynamic adjustement of acceptance ratio and sector angle

One of the key parameters of our simulations is the **acceptance ratio**. It measures the number of accepted Metropolis moves relative to the number of proposed Metropolis moves (it does not count over-relaxation moves, which are always accepted). The chosen compromise is to try to reach a ratio of 50%, for two main reasons:

- To ensure efficient exploration of the phase space.
- To minimize biases introduced by non-representative move proposals.

Thus, a too low acceptance ratio indicates that the proposed moves are too large, leading to frequent Metropolis rejections: the Markov chain does not progress, gets stuck, and does not converge during the warmup, which then fails. The exploration is not representative of the real physics during the measurement phase. Conversely, a too high acceptance ratio indicates that the proposed moves are too small, leading to inefficient exploration of phase space: the Markov chain converges too quickly to the wrong equilibrium and remains stuck there, the warmup fails, and we still do not explore the real physics during the measurement phase.

The two key parameters that control the value of the acceptance ratio are obviously the angle θ of the Gaussian used for Metropolis moves, and the current temperature T . A dynamically decreasing exponential formula was chosen for adapting the angle θ during the warmup, as presented in 2.3.2.

$$\theta \leftarrow \theta \times \exp \left(\frac{1}{\sqrt{N_{adapt}}} \cdot (r_{avg} - 0.5) \right)$$

The exponential allows for a rapid response, and the dynamically decreasing adaptation in $1/\sqrt{N_{adapt}}$ ensures certain convergence (the value of N_{adapt} is reset to zero at the start of each phase 2).

We inevitably observe in Figure 13 a slight relaxation time at the start of each phase 2 for each cooling temperature:

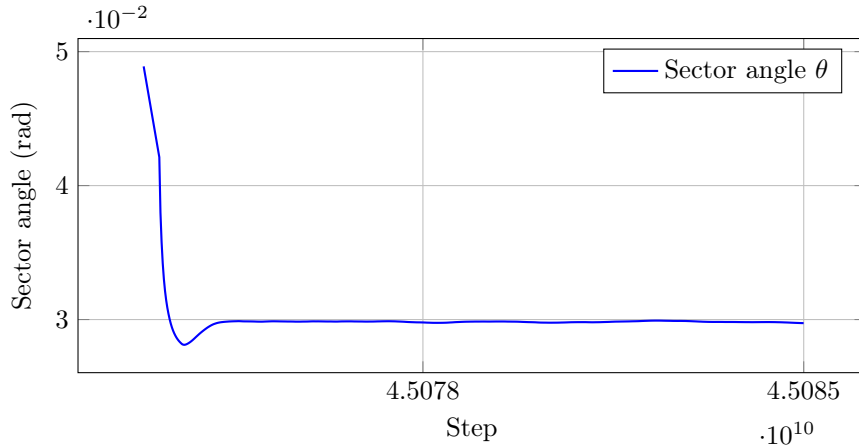


Figure 13: **Relaxation time** of the sector angle evolution during the warmup phase, at the last cooling stage at $T = 0.0005$ for $L = 150$ and $J_1 = -1.0, J_2 = 0.5, J_3 = 0.25$. Relaxation is inevitable because the sector angle is not yet adapted from the previous cooling temperature: since we move to a lower temperature, the acceptance ratio drops, and the sector angle must be decreased in response. The exponential does this relatively abruptly, but it is quickly damped and ends up converging very precisely. The curve has 566 points that have been connected, and a zoom on the damping has been made. This cooling stage actually ends at step number 5.1071e10, but is cut here at step number 4.5085e10 for readability.

Below are some statistics on the acceptance ratio obtained at the end of the warmup, which further demonstrate its robustness.

Table 2: Acceptance ratio statistics in phase 3 of each cooling stage (target temperature $T = 0.0005$) with sector angle θ mean values and number of points n

k	$T_{cool}[k]$	mean acc ratio	std	min	max	mean θ	n
0	0.500500	0.501081	0.000794	0.499633	0.502462	1.133610	333
1	0.186539	0.501733	0.001038	0.499926	0.503542	0.599320	961
2	0.069524	0.502137	0.001243	0.498676	0.504241	0.357528	1195
3	0.025912	0.502315	0.001369	0.499335	0.504686	0.215985	1282
4	0.009658	0.502350	0.001404	0.499384	0.504752	0.131467	1315
5	0.003599	0.502331	0.001409	0.499780	0.504778	0.080163	1327
6	0.001342	0.502370	0.001473	0.499225	0.504903	0.048899	1332
7	0.000500	0.502399	0.001472	0.499139	0.504925	0.029841	1333

Table 3: Acceptance ratio statistics in phase 3 of each cooling stage ($T = 1.0$), with sector angle θ mean values and number of points n

k	$T_{cool}[k]$	mean acc	std	min	max	mean θ	n
0	1.50000	0.5885	0.00009	0.5885	0.5894	3.1416	333
1	1.31487	0.5544	0.00007	0.5543	0.5550	3.1416	704
2	1.18222	0.5270	0.00004	0.5266	0.5272	3.1416	969
3	1.09329	0.5072	0.00006	0.5066	0.5073	3.1416	1147
4	1.03936	0.5000	0.00005	0.4998	0.5010	3.0734	1254
5	1.01166	0.4999	0.00010	0.4966	0.5007	2.9958	1311
6	1.00146	0.5000	0.00004	0.4998	0.5009	2.9664	1331
7	1.00000	0.4999	0.00003	0.4990	0.5000	2.9637	1333

Note: The acceptance ratio is closely linked to the Boltzmann probability $\mathbb{P} \propto \exp\left(-\frac{\Delta E}{k_B T}\right)$ present in Metropolis moves. This remains close to 0.5, but the value of ΔE is highly dependent on the angle θ , which is, for example, about 1.7 degrees for $T = 0.0005$, about 80 degrees for $T = 0.4$ for the same parameters as in Figure 13. We notice from Table 3 that we can no longer reach 50% acceptance between $T = 1.09329$ and $T = 1.03936$: the ratio is $> 50\%$ and the angle θ is at its maximum bound π . There is nothing we can do about it, and it is not a bad thing in this case, it is simply the physics of the system! We also notice from Table 2 that the global moves proposed with the activation of the **Low T Protocol** (see section 1) make the acceptance ratio fluctuate more, naturally increasing its variance, but only very slightly, and this is not a problem! Such extreme precision is of course not necessary for thermalization, but it provides statistical comfort.

3.1.2 Successive configurations during cooling

The best way to test the robustness of the warmup is to check the final configuration reached at very low temperature, i.e., well below $T = 0.1$. It is in this regime that it is most difficult to escape metastable states. Below in Figure 14 we show three cooling stages for the final temperature $T = 0.0005$ and three for the final temperature $T = 0.0007$.

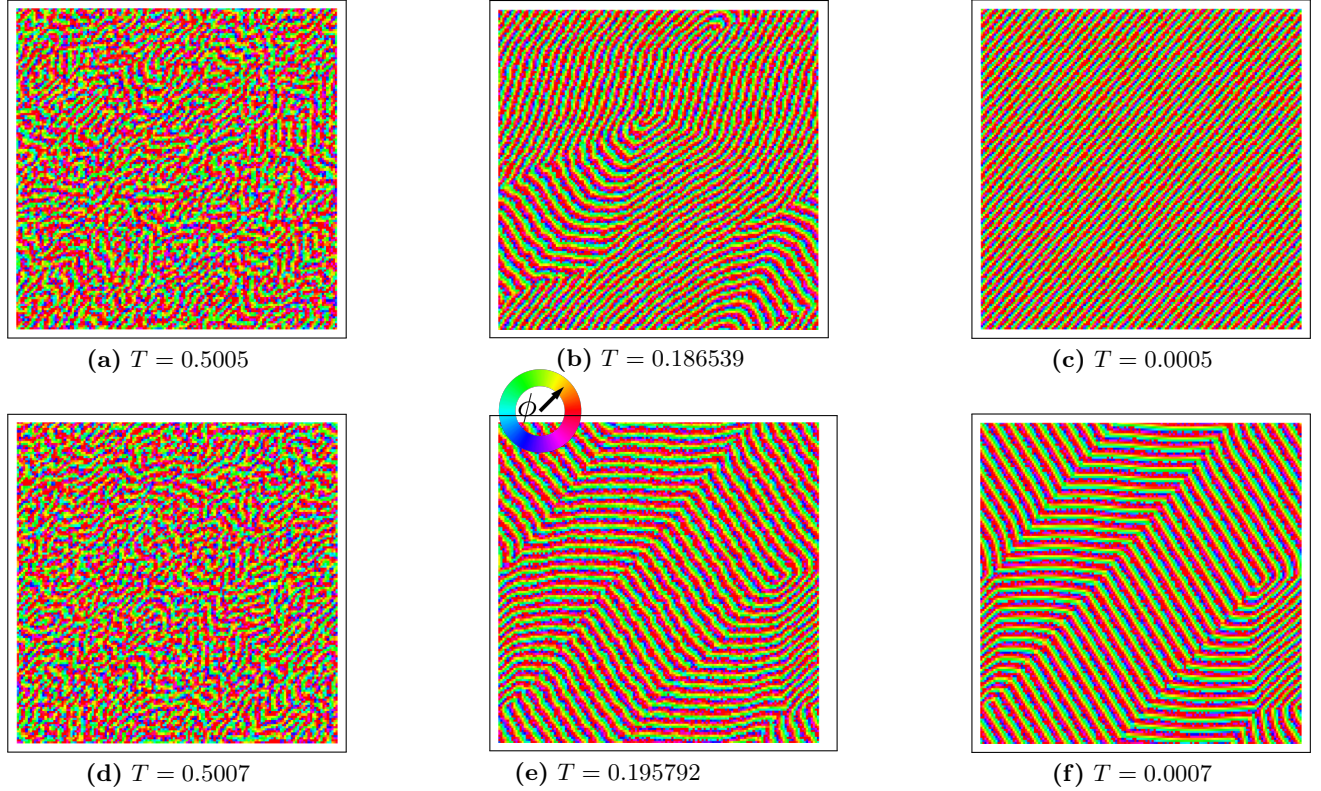


Figure 14: Cooling stages $T_{cool}[0]$, $T_{cool}[1]$ and $T_{cool}[7]$ for final temperatures $T = 0.0005$ (top) and $T = 0.0007$ (bottom). The first row shows an ideal warmup, where only a single wave vector is selected (perfect spiral-ordered state). The second row shows typical configurations reached at very low but nonzero temperatures, where usually two wave vectors are selected. This is a very weak metastable state, which is still acceptable if one of the two wave vectors is clearly dominant (as is the case here, see 15). $L = 150$, $(J_1, J_2, J_3) = (-1, 0.50, 0.25)$ in both cases.

In Figure 15 are the final configurations for the two temperatures $T = 0.0005$ and $T = 0.0007$, with their corresponding structure factor:

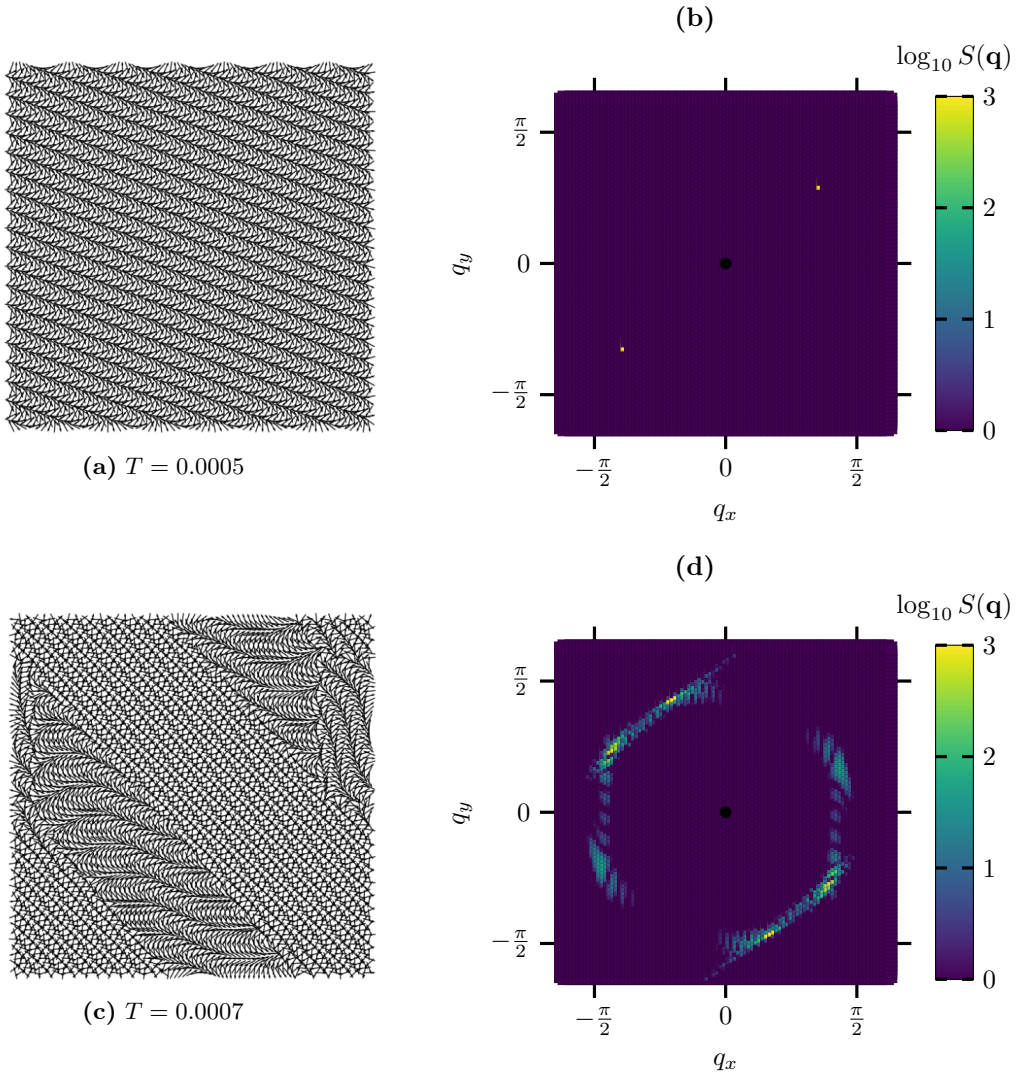


Figure 15: Left column: Spin orientations (one spin out of two shown for clarity). Right column: Corresponding structure factor for $T = 0.0005$ (top) and $T = 0.0007$ (bottom). For $T = 0.0005$, the warmup phase worked perfectly and the system selected a single wave vector \vec{q}_0 (perfect spiral-ordered state, see Section 1.6). For $T = 0.0007$, the system remained in a slightly metastable state with two main wave vectors \vec{q}_1 and \vec{q}_2 and some fluctuations. This is an example of imperfect thermalization, which can happen, but rarely and mainly at very low temperature.

3.1.3 Conclusion on the warmup phase

We manage to adapt the sector angle θ very precisely throughout the cooling to reach an ultra-stabilized acceptance ratio at 50% (section 3.1.1). In fact, such precision is not really necessary, but it is a guarantee of exemplary reproducibility of the simulations: nothing is left to chance regarding the initial configuration. The risk of ending thermalization in a metastable state will never be zero, especially at very low temperature (Figure 14). However, we try as much as possible to average each point over several independent simulations, which is the best way to obtain reliable results. One could criticize the fact that in Table 1 the duration percentages are not reversed between high and low temperature regimes (we would want a duration that quickly becomes longer at low temperature, during geometric cooling). But the warmup duration remains in any case very long (tens of billions of steps for the entire cooling). Overall, the robustness of the warmup is **very satisfactory**.

3.2 Berezinskii-Kosterlitz-Thouless phase transition for various lattice sizes

The goal of this section is to determine, as precisely as possible, the temperature of the Berezinskii-Kosterlitz-Thouless (BKT) transition in the thermodynamic limit $L \rightarrow \infty$.

3.2.1 Large scan in temperature of main observables

We start by roughly locating the transition with a scan over a wide range of temperatures. This also helps confirm which observable is most relevant for studying this transition. The graphs in Figure 16 were produced with our algorithm for a lattice size $L = 80$ and temperatures from $T = 0.1$ to $T = 2.5$, with a step of 0.1 except near the transition, where the step is 0.05.

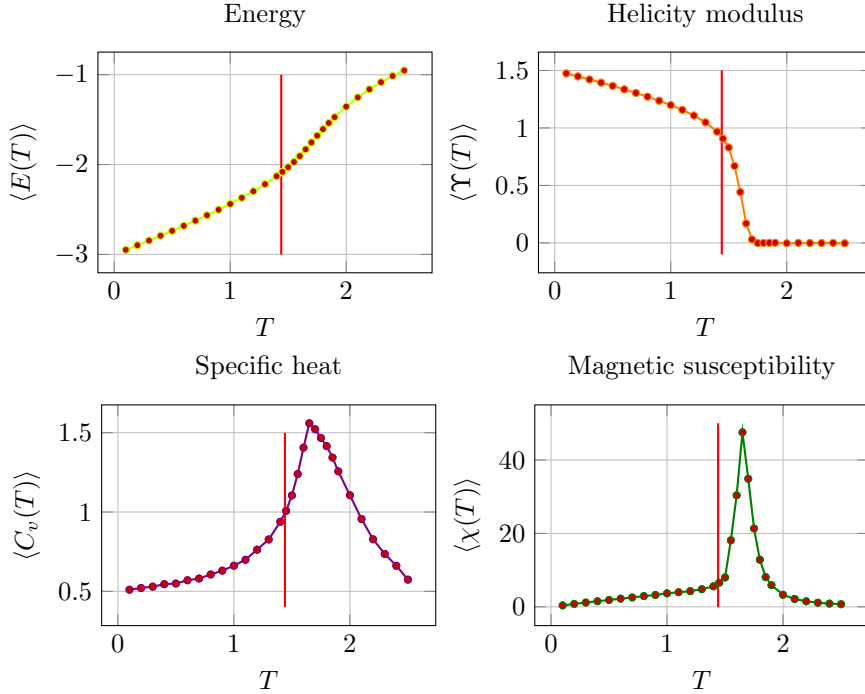


Figure 16: Main observables (energy, helicity modulus, specific heat, and magnetic susceptibility, see 2.4 for their computation) as a function of temperature for $L = 80$ in the pure ferromagnetic case $J_1 = J = -1$. The thin red vertical line marks $T = 1.44$, the approximate BKT transition temperature, at the intersection between the $2T/\pi$ curve and the Υ curve (see section 1.2). Simulations were run from $T = 0.1$ to $T = 2.5$, with a step of 0.1 except near the transition, where the step is 0.05. The aim here is to get a global view, so each point is not averaged over several independent simulations, and the temperature step is much larger than in the following simulations.

We notice something subtle and interesting: the precise location of the BKT transition is at a *lower* temperature than the peaks in the specific heat and magnetic susceptibility. This is related to the *topological* nature of the transition. These two observables are sensitive to the maximum proliferation of free vortices, whereas the transition itself corresponds to the sudden unbinding of vortex-antivortex pairs. This is why it is important to use the helicity modulus Υ to detect the BKT transition! The transition is easily visible for $J_2 = J_3 = 0$, and shifts to lower temperatures as frustration from J_2 and J_3 increases

3.2.2 Looking for unbinding of vortex-antivortex pairs in real space

It is tempting to visualize vortex-antivortex pairs and their unbinding above the transition temperature. However, the BKT transition occurs around $T = 1.44$, which is already a very high temperature for our system. As seen in Figure 14, even at $T = 0.5$ the spin configuration is already highly disordered. Near the BKT transition, thermal fluctuations are even stronger, making it very difficult to clearly see vortices and antivortices in real space, especially for finite-size systems. For examples of spin configurations near the BKT transition, see section 3.3.2.

3.2.3 Estimated value for transition temperature in the thermodynamic limit

Theory predicts the following formula for the dependence of the BKT transition temperature on L :

$$T_{\text{BKT}}(L) = T_{\text{BKT}}^{\infty} + \frac{A}{\ln(L/L_0)^2}, \quad (8)$$

where T_{BKT}^∞ is the transition temperature in the thermodynamic limit, and A and L_0 are constants [10].

From Figure 16, we get an idea of $T_{\text{BKT}}(L)$, which is known to be only weakly dependent on L . We can then run simulations for several lattice sizes L over a very narrow temperature interval, with a fine temperature step, to estimate several values of $T_{\text{BKT}}(L)$ and then extract T_{BKT}^∞ using a nonlinear least squares method. See Figure 17 for $L = 100$ and $L = 150$.

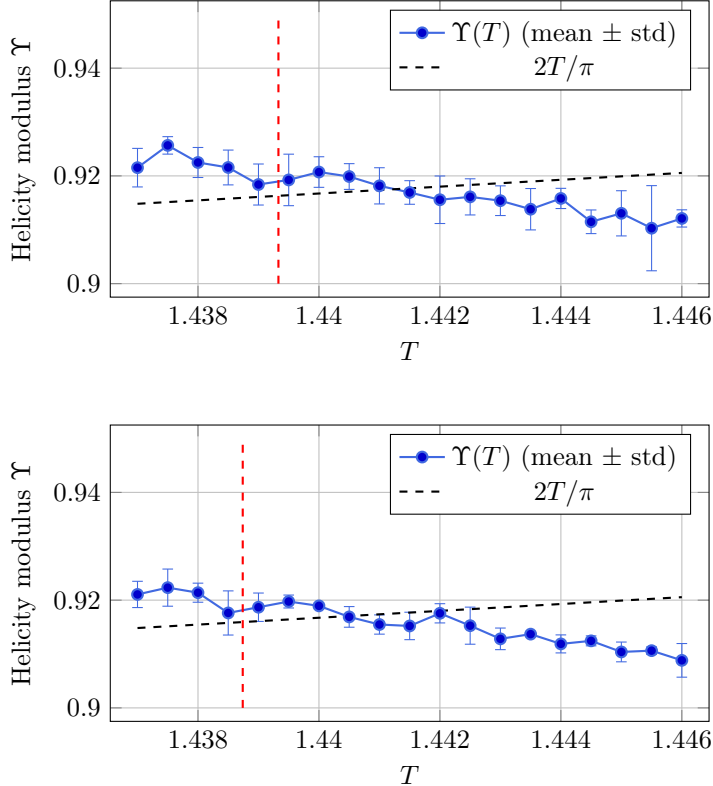


Figure 17: Helicity modulus $\Upsilon(T)$ for $L = 100$ (top) and $L = 150$ (bottom). The blue curve is the mean value with error bars (each point is averaged over 10 independent simulations and separated by a 0.0005 step in temperature). The dashed black line is $2T/\pi$, and the red dashed line marks the BKT transition temperature T_{BKT} , detected by linear interpolation at the first crossing of $2T/\pi$ and $\Upsilon \pm \text{std}$. See Appendix 3.3.2 for details. We observe that the transition occurs at a slightly lower temperature for the bottom curve at $L = 150$. The slow decrease of the function $L \mapsto T_{\text{BKT}}(L)$ can be seen here and was clearly demonstrated for different lattice sizes.

This type of simulation was repeated for different lattice sizes. The results are summarized in the table below.

Table 4: Estimated BKT transition temperature T_{BKT} as a function of lattice size L .

L	50	60	70	75
$T_{\text{BKT}} \pm \text{std}$	1.4447 ± 0.0005	1.4435 ± 0.0005	1.4425 ± 0.0006	1.4410 ± 0.0009
L	100	110	125	150
$T_{\text{BKT}} \pm \text{std}$	1.4393 ± 0.0007	1.4392 ± 0.0008	1.4392 ± 0.0010	1.4387 ± 0.0017

The least squares method for fixed $L_0 = 1$ gives:

$$T_{\text{BKT}}^\infty = 1.42693 \pm 0.00177 \quad A = 0.27409 \pm 0.03146 \quad (9)$$

If L_0 is treated as a free parameter, the results are less precise:

$$T_{\text{BKT}}^\infty = 1.42772 \pm 0.01608 \quad A = 0.23237 \pm 0.80537 \quad L_0 = 1.259 \pm 5.902 \quad (10)$$

The maximum value of T_{BKT}^∞ is 1.4438, which is clearly inconsistent with the decreasing trend observed in Table 4, motivating the use of the fixed value $L_0 = 1$.

In all cases, the uncertainties on the $\Upsilon(T)$ curve and thus on $T_{\text{BKT}}(L)$ are quite large and only allow a precise estimate up to the second decimal place. But the literature found that $T_{\text{BKT}}^{\infty} = 1.43$ ([10]) which is very consistent with our findings. We finally conclude that $T_{\text{BKT}}(L)$ decreases with L , and we have a clear idea of the transition temperature for even better future statistics in the pure ferromagnetic case in the thermodynamic limit. With more time, I would have increased the total number of steps, further improved the warmup phase, and averaged over more simulations.

3.3 Localization of lattice rotational symmetry-breaking $\mathcal{C}_6 \rightarrow \mathcal{C}_2$

3.3.1 Characterization of the nematic spiral phase with a heatmap of the \mathcal{O}_6 order parameter

We test the $\mathcal{C}_6 \rightarrow \mathcal{C}_2$ symmetry breaking for 13,794 pairs (T, δ) , with $\delta = J_2 - 0.20$. The temperature varies from 0.0001 to 0.0009 in steps of 0.0001, then from 0.001 to 0.005 in steps of 0.001, and finally from 0.005 to 0.5 in steps of 0.05. The parameter δ varies from 0.0025 to 0.30 in steps of 0.0025. The lattice size is $L = 150$, and we stay on the line $J_3 = J_2/2$, which is a necessary condition for the appearance of the SSL (see section 1.6).

Here is a plot of $\mathcal{O}_6(T)$ for $\delta = 0.20$ (i.e., $J_2 = 0.40$ and $J_3 = J_2/2$) with the structure factor $S(\mathbf{q})$ before and after the transition:

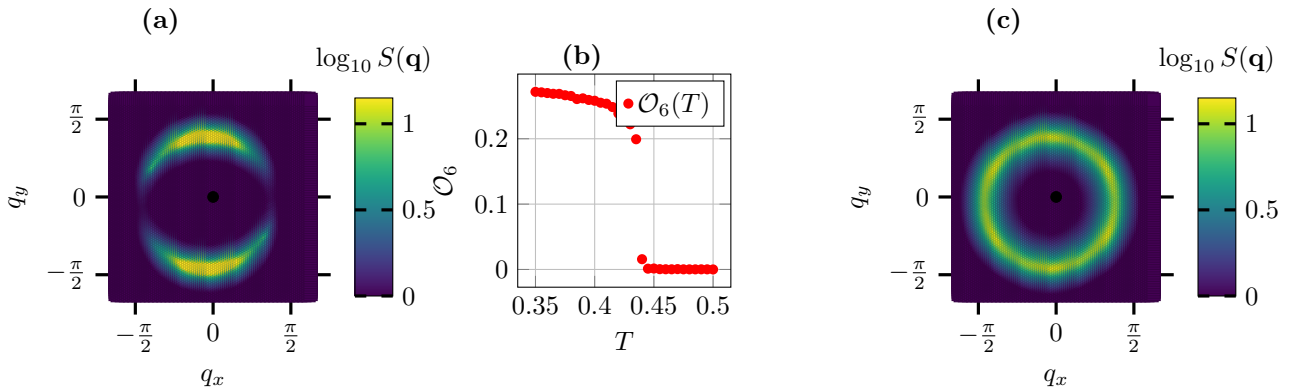


Figure 18: (a) Structure factor $S(\mathbf{q})$ at $T = 0.425$ in the nematic phase where the order parameter \mathcal{O}_6 is non zero. We can see a momentum arc as explained in section 1.6; (b) Order parameter $\mathcal{O}_6(T)$ for $\delta = 0.20$; (c) Structure factor $S(\mathbf{q})$ at $T = 0.435$ in the spiral spin liquid phase where the order parameter \mathcal{O}_6 is zero, the \mathcal{C}_6 is restored and the system explore a continuous hexagon ring in momentum space.

In this case, we find $T_c \approx 0.43 \pm 0.005$ where \mathcal{O}_6 vanishes. Then is the cartography of the \mathcal{O}_6 order parameter in the (T, δ) plane:

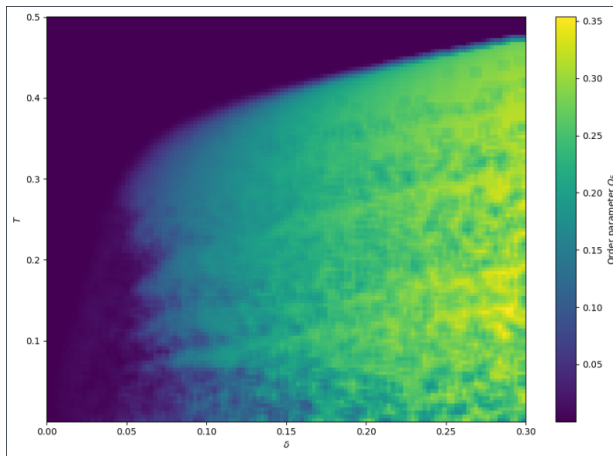


Figure 19: Heatmap of the \mathcal{O}_6 order parameter as a function of temperature T and the frustration parameter δ . Each point is averaged over neighboring points to smooth the heatmap, but I checked that this does not affect the critical regions, so the physics is unchanged. The nematic spiral phase corresponds to regions where $\mathcal{O}_6 > 0$, the spiral spin liquid (SSL) to regions where it is zero. See [9] for an heatmap of the same order parameter in the square geometry.

Visually, we estimate a critical value $\delta_c = 0.05 \pm 0.02$ above which symmetry breaking is clearly observed. What happens for lower values of δ is not clear; the boundary is not straight and we are probably in an intermediate spiral-disordered phase between the nematic phase and the spiral spin liquid phase (see section 1.6). The critical transition temperature depends on δ .

3.3.2 Looking for momentum vortices in real space

The transition from the nematic spiral phase to the spiral spin liquid phase occurs with the loss of long-range order (forbidden by the Mermin-Wagner theorem but visible at finite size), and the loss of preferred orientations, which reveals momentum vortices in real space:

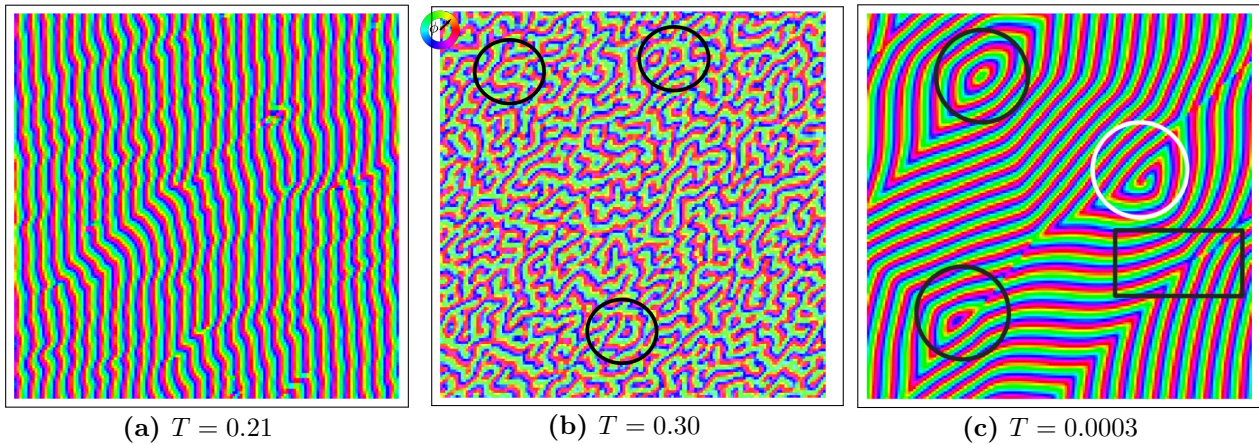


Figure 20: (a) We are clearly in the nematic spiral phase with long-range order and a clear preferred orientation of the spins. (b) Spiral spin liquid phase, showing what strongly looks like momentum vortices, circled in black. See (c) for clear examples of momentum vortices (circled in black) and an anti-vortex (boxed in black) in real space. What is circled in white is a spin vortex (see section 1.2) combined with a momentum vortex. (c) is a configuration obtained by a simulation at very low temeprature ($T = 0.0003$) for better visualization. All three configurations were quenched (see section 2.2.2). $L = 150$, $J_2 = 0.27$ ($\delta = 0.07$), $J_3 = 0.135$ except (c) which is $L = 150$, $J_2 = 0.50$ ($\delta = 0.30$), $J_3 = 0.25$.

Conclusion

In this work, I first learned to master the C++ language and the large-scale classical Monte Carlo method. I used these skills to simulate frustrated or purely ferromagnetic magnetic systems at finite temperature with triangular geometry. I clearly showed the nematic spiral and spiral spin liquid phases in section 3.3.1. I managed to observe vortices and anti-vortices of moments in real space in Figure 8, even though their existence is still unclear in triangular geometry, and spin vortices in Figure 20. I also detected the Berezinskii-Kosterlitz-Thouless transition with good precision in section 3.2.3, and its value in thermodynamic limit $T_{\text{BKT}}^\infty = 1.42772 \pm 0.01608$ is consistent with litterature. All these simulations rely on a robust warmup phase that can be trusted, described in section 2.3.2. However, it can still be improved (see Figure 14) to get perfect results. With more time, I would improve this warmup phase, increase the already long measurement phase of $500,000 \times L^2$ steps, and average each point over more independent simulations (currently, each point in Figure 17 is averaged over 10 independent simulations). We observed clear momentum vortices at finite temperatures for finite-size lattices ($L = 150$), as shown in Figure 20. While their presence in the thermodynamic limit remains an open question, our results provide strong evidence for their existence in the triangular geometry. Finally, we resolved the continuous transition from the nematic to the spiral spin liquid phase over a large region of the (J_2, T) phase diagram; however, the behavior of the order parameter \mathcal{O}_6 and the nature of the phases at temperatures $T < 0.3$ and $\delta < 0.07$ remain open questions for future investigation.

Appendix A

Fourier transform of the Hamiltonian

We provide here a derivation of the momentum-space representation of the Hamiltonian using the Fourier transform of the spin field. This method is useful at finite temperature to deduce the class of wave vectors

which minimizes the energy.

We define the discrete Fourier transform as:

$$\vec{S}_{\vec{q}} = \frac{1}{\sqrt{N}} \sum_i \vec{S}_i e^{-i\vec{q} \cdot \vec{r}_i}, \quad \vec{S}_i = \frac{1}{\sqrt{N}} \sum_{\vec{q}} \vec{S}_{\vec{q}} e^{i\vec{q} \cdot \vec{r}_i}.$$

We now rewrite the Hamiltonian in terms of spin scalar products:

$$\mathcal{H} = \sum_{i,j} J(\vec{r}_i - \vec{r}_j) \vec{S}_i \cdot \vec{S}_j.$$

Substituting the inverse Fourier transforms of \vec{S}_i and \vec{S}_j gives:

$$\vec{S}_i \cdot \vec{S}_j = \frac{1}{N} \sum_{\vec{q}, \vec{q}'} \vec{S}_{\vec{q}} \cdot \vec{S}_{\vec{q}'} e^{i\vec{q} \cdot \vec{r}_i} e^{i\vec{q}' \cdot \vec{r}_j},$$

and therefore:

$$\mathcal{H} = \frac{1}{N} \sum_{\vec{q}, \vec{q}'} \vec{S}_{\vec{q}} \cdot \vec{S}_{\vec{q}'} \sum_{i,j} J(\vec{r}_i - \vec{r}_j) e^{i\vec{q} \cdot \vec{r}_i} e^{i\vec{q}' \cdot \vec{r}_j}.$$

We now change variables by defining the displacement vector $\vec{\delta} = \vec{r}_i - \vec{r}_j$, so that $\vec{r}_j = \vec{r}_i - \vec{\delta}$, and the double sum becomes:

$$\sum_{i,j} J(\vec{r}_i - \vec{r}_j) e^{i\vec{q} \cdot \vec{r}_i} e^{i\vec{q}' \cdot \vec{r}_j} = \sum_{i, \vec{\delta}} J(\vec{\delta}) e^{i\vec{q} \cdot \vec{r}_i} e^{i\vec{q}' \cdot (\vec{r}_i - \vec{\delta})} = \sum_{i, \vec{\delta}} J(\vec{\delta}) e^{i(\vec{q} + \vec{q}') \cdot \vec{r}_i} e^{-i\vec{q}' \cdot \vec{\delta}}.$$

The sum over i gives a Kronecker delta enforcing momentum conservation:

$$\sum_i e^{i(\vec{q} + \vec{q}') \cdot \vec{r}_i} = N \delta_{\vec{q} + \vec{q}', 0},$$

and so the Hamiltonian becomes:

$$\mathcal{H} = \sum_{\vec{q}} \left[\sum_{\vec{\delta}} J(\vec{\delta}) e^{i\vec{q} \cdot \vec{\delta}} \right] \vec{S}_{-\vec{q}} \cdot \vec{S}_{\vec{q}}.$$

We define the momentum-dependent coupling as:

$$J(\vec{q}) = \sum_{\vec{\delta}} J(\vec{\delta}) e^{i\vec{q} \cdot \vec{\delta}},$$

which leads to:

$$\mathcal{H} = \sum_{\vec{q}} J(\vec{q}) \vec{S}_{-\vec{q}} \cdot \vec{S}_{\vec{q}}.$$

To go further, since spins are real vectors, we can use the property $\vec{S}_{-\vec{q}} = \vec{S}_{\vec{q}}^*$ to write the final compact form:

$$\boxed{\mathcal{H} = \sum_{\vec{q}} J(\vec{q}) |\vec{S}_{\vec{q}}|^2.}$$

Fluctuation formula for the specific heat

We briefly show that the specific heat can be expressed as the fluctuations of the energy in the canonical ensemble:

$$C_v = \frac{\partial \langle E \rangle}{\partial T}.$$

Let $\mathcal{Z} = \sum_{\{s\}} e^{-\beta \mathcal{H}(s)}$ be the partition function, $\beta = 1/T$ (with $k_B = 1$). The average energy is

$$\langle E \rangle = \frac{1}{\mathcal{Z}} \sum_{\{s\}} E(s) e^{-\beta \mathcal{H}(s)}.$$

Taking the derivative with respect to T :

$$C_v = \frac{\partial \langle E \rangle}{\partial T} = -\frac{1}{T^2} \frac{\partial \langle E \rangle}{\partial \beta}.$$

But using the formula with the partition function,

$$\frac{\partial \langle E \rangle}{\partial \beta} = -(\langle E^2 \rangle - \langle E \rangle^2),$$

so

$$C_v = \frac{1}{T^2} (\langle E^2 \rangle - \langle E \rangle^2) = \beta^2 (\langle E^2 \rangle - \langle E \rangle^2),$$

which is the desired fluctuation formula.

Paramagnetic behavior exploration via Central limit theorem

In the paramagnetic phase, at high temperature, thermal fluctuations dominate and the spins are essentially uncorrelated. Each spin \vec{S}_i can be considered as an independent random unit vector in the plane, with its angle ϕ_i uniformly distributed in $[0, 2\pi]$.

The total magnetization is defined as:

$$\vec{M} = \sum_{i=1}^N \vec{S}_i = \left(\sum_{i=1}^N \cos \phi_i, \sum_{i=1}^N \sin \phi_i \right).$$

Since the ϕ_i are independent and uniformly distributed, both $\sum \cos \phi_i$ and $\sum \sin \phi_i$ are sums of independent random variables of mean zero and variance $N/2$.

By the Central Limit Theorem, for large N , the components of \vec{M} are approximately Gaussian with mean zero and variance $N/2$. The modulus $|\vec{M}|$ then follows a Rayleigh distribution with parameter $\sigma^2 = N/2$.

The mean value of the modulus is:

$$\langle |\vec{M}| \rangle = \sigma \sqrt{\frac{\pi}{2}} = \sqrt{\frac{N}{2}} \sqrt{\frac{\pi}{2}} = \frac{\sqrt{\pi N}}{2}.$$

Normalizing by the number of spins N , the average magnetization per spin is:

$$\langle M \rangle = \frac{\langle |\vec{M}| \rangle}{N} = \frac{\sqrt{\pi}}{2} \cdot \frac{1}{\sqrt{N}} \approx \frac{0.886}{\sqrt{N}}.$$

This result shows that, in the paramagnetic phase, the magnetization vanishes as N increases, following a $1/\sqrt{N}$ law. This scaling is a direct consequence of the Central Limit Theorem applied to independent spins, and is observed in simulations as well as in theory.

For example, for $N = 2500$ ($L = 50$), we expect $\langle M \rangle \approx 0.0177$ (which has been successfully observed).

Derivation of the computed structure factor formula

We start from the definition of the structure factor:

$$S(\vec{q}) = \frac{1}{N} \sum_{i,j} \vec{S}_i \cdot \vec{S}_j e^{i\vec{q} \cdot (\vec{r}_j - \vec{r}_i)}.$$

The scalar product between two spins can be written as $\vec{S}_i \cdot \vec{S}_j = S_i^x S_j^x + S_i^y S_j^y$. Therefore, the structure factor becomes:

$$S(\vec{q}) = \frac{1}{N} \sum_{i,j} S_i^x S_j^x e^{i\vec{q} \cdot (\vec{r}_j - \vec{r}_i)} + \sum_{i,j} S_i^y S_j^y e^{i\vec{q} \cdot (\vec{r}_j - \vec{r}_i)}.$$

We can separate the two double sums to make the complex conjugate structure explicit (the indices i and j are dummy variables):

$$S(\vec{q}) = \frac{1}{N} \sum_i S_i^x e^{-i\vec{q} \cdot \vec{r}_i} \sum_j S_j^x e^{i\vec{q} \cdot \vec{r}_j} + \sum_i S_i^y e^{-i\vec{q} \cdot \vec{r}_i} \sum_j S_j^y e^{i\vec{q} \cdot \vec{r}_j}.$$

We immediately see that

$$S(\vec{q}) = \frac{1}{N} \left| \sum_i S_i^x e^{i\vec{q} \cdot \vec{r}_i} \right|^2 + \left| \sum_i S_i^y e^{i\vec{q} \cdot \vec{r}_i} \right|^2.$$

This shows that $S(\vec{q})$ is the sum of the squared modulus of the Fourier transforms of the real spin components S^x and S^y . Numerically, we compute the discrete Fourier transforms:

$$\hat{S}^x(\vec{q}) = \sum_i S_i^x e^{-i\vec{q} \cdot \vec{r}_i}, \quad \hat{S}^y(\vec{q}) = \sum_i S_i^y e^{-i\vec{q} \cdot \vec{r}_i}$$

and the normalized structure factor is then given by:

$$S(\vec{q}) = \frac{1}{N} \left(|\hat{S}^x(\vec{q})|^2 + |\hat{S}^y(\vec{q})|^2 \right).$$

In practice, we average over multiple configurations to obtain a reliable estimate of the structure factor, then we always work with:

$$S(\vec{q}) = \frac{1}{N} \left\langle |\hat{S}^x(\vec{q})|^2 + |\hat{S}^y(\vec{q})|^2 \right\rangle.$$

Reciprocal lattice vectors for the triangular lattice

Given the direct lattice basis vectors

$$\vec{a}_1 = (1, 0), \quad \vec{a}_2 = \left(\frac{1}{2}, \frac{\sqrt{3}}{2} \right),$$

the reciprocal lattice vectors are

$$\vec{b}_1 = \frac{4\pi}{\sqrt{3}} \left(\frac{\sqrt{3}}{2}, -\frac{1}{2} \right), \quad \vec{b}_2 = \frac{4\pi}{\sqrt{3}} (0, 1),$$

obtained by the standard formula

$$\vec{b}_1 = 2\pi \frac{\vec{a}_2 \times \vec{a}_3}{\vec{a}_1 \cdot (\vec{a}_2 \times \vec{a}_3)}, \quad \vec{b}_2 = 2\pi \frac{\vec{a}_3 \times \vec{a}_1}{\vec{a}_1 \cdot (\vec{a}_2 \times \vec{a}_3)},$$

with $\vec{a}_3 = (0, 0, 1)$ unit vector perpendicular to the plane.

The reciprocal lattice is thus a clockwise rotation of the direct lattice by 30° and is scaled by a factor $4\pi/\sqrt{3}$.

Appendix B

Old inefficient warmup method

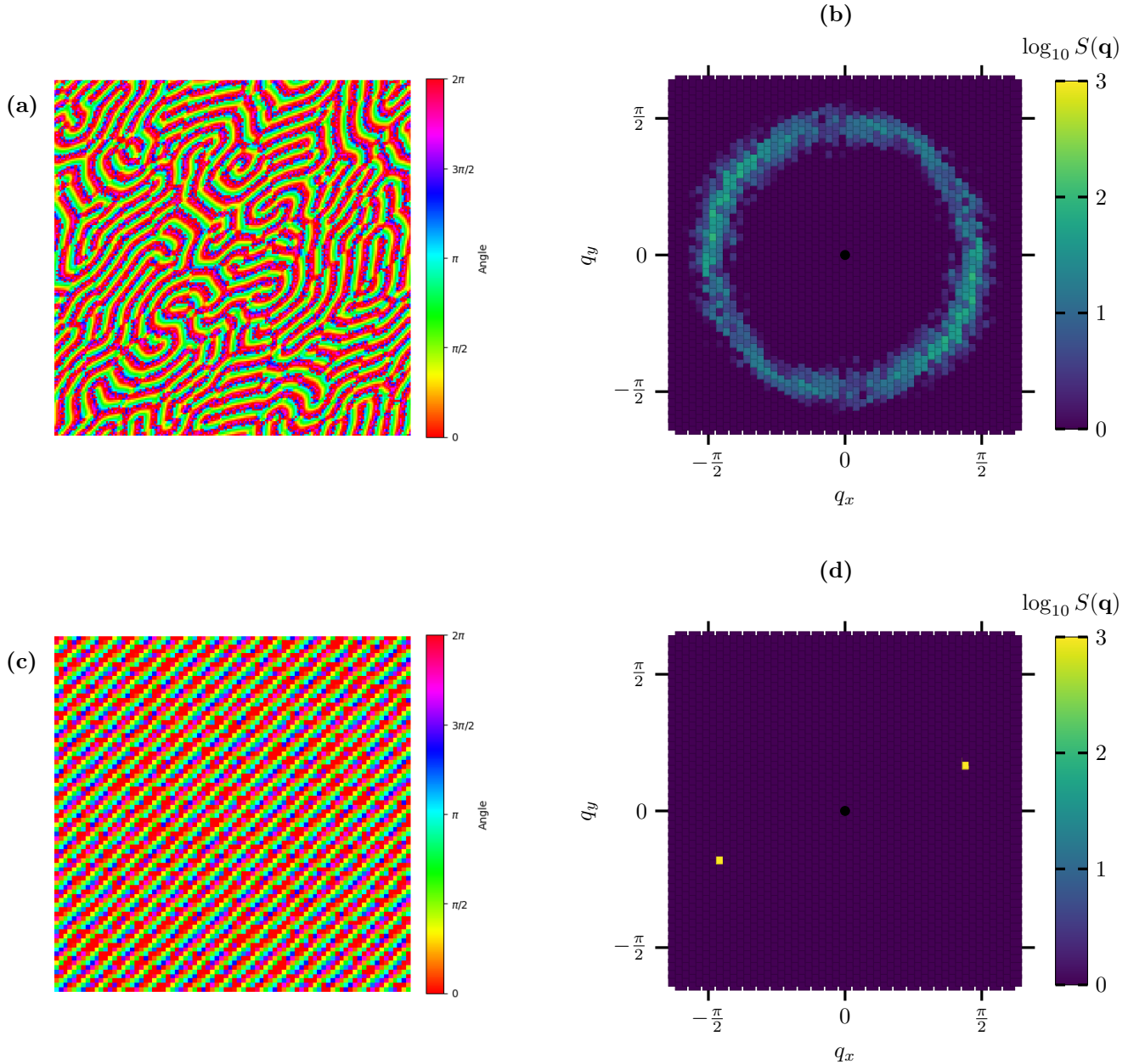


Figure 21: (a) and (c) show real-space spin configurations at $T = 0.0001$, $L = 200$ (with a quench applied in Python for better visualization). (b) and (d) show the corresponding structure factors $S(\mathbf{q})$ (log scale). In (a), the configuration is not the expected one at such low temperature: several wave vectors are selected on a ring, and a symmetric arc can be seen in (b). This is a spiral-disordered, almost nematic phase, which is a clear sign of a metastable state at this temperature. In (c), the spins clearly form an ordered spiral, with the phase varying linearly along a single direction, corresponding to a unique selected wave vector. This first configuration (a) showed me that even my advanced warmup code was not robust enough at very low temperature. Technical improvements were made, especially by adding a cooling method in the warmup phase.

Appendix C

Warmup statistics for a typical temperature of simulation near BKT transition

Table 5: Acceptance ratio statistics in phase 3 of each cooling stage (target temperature $T = 1.4$)

k	$T_{cool}[k]$	mean	std	min	max	n
0	1.90000	0.648676	0.000074	0.648028	0.648740	333
1	1.71487	0.622824	0.000072	0.622734	0.624351	704
2	1.58222	0.602129	0.000046	0.601747	0.602513	969
3	1.49329	0.587236	0.000092	0.584392	0.587617	1147
4	1.43936	0.577727	0.000024	0.577550	0.578150	1254
5	1.41166	0.572681	0.000101	0.569131	0.572877	1311
6	1.40146	0.570900	0.000067	0.570608	0.571760	1331
7	1.40000	0.570568	0.000040	0.570372	0.570948	1333

Spins configuration near BKT transition. Attempt to visualize vortices and antivortices, but thermal fluctuations are too strong.

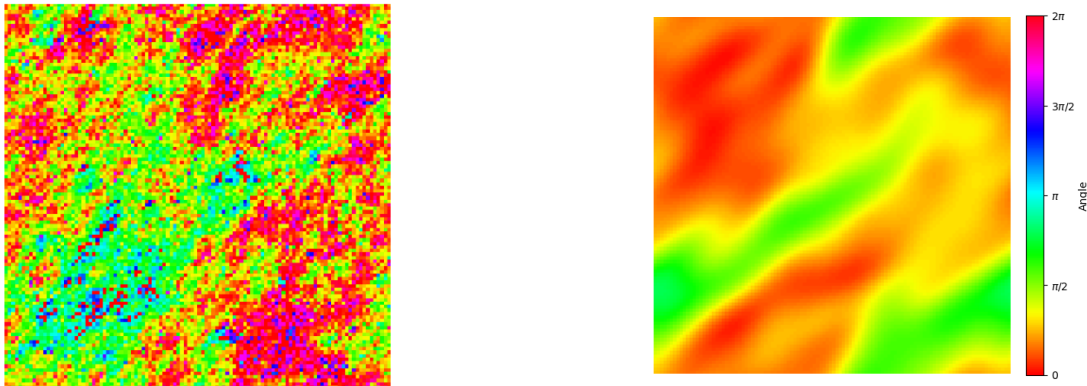


Figure 22: Left: spin configuration without quench (see section 2.2.2 for quench method) and *before* BKT transition. Right: spin configuration after quench, and *after* BKT transition. Quench makes free vortices totally disappear.

Linear interpolation method for determining T_{BKT}

To estimate the transition temperature T_{BKT} precisely, we find the first interval $[T_{i-1}, T_i]$ where the observable curve (for example, the helicity modulus Υ) crosses the theoretical curve (for example, $2T/\pi$). We assume both curves are linear in this interval and solve

$$y_{\text{obs}}(T) = y_{\text{th}}(T),$$

by linear interpolation:

$$T_{BKT} = T_{i-1} + \frac{y_{\text{th}}(T_{i-1}) - y_{\text{obs}}(T_{i-1})}{\left[\frac{y_{\text{obs}}(T_i) - y_{\text{obs}}(T_{i-1})}{T_i - T_{i-1}} - \frac{y_{\text{th}}(T_i) - y_{\text{th}}(T_{i-1})}{T_i - T_{i-1}} \right]},$$

where $y_{\text{obs}}(T)$ and $y_{\text{th}}(T)$ are the values of the observable and the theoretical curve at temperatures T_{i-1} and T_i .

The uncertainty on T_{BKT} is estimated by repeating the interpolation with the extreme values of the observable (mean \pm standard deviation), and then taking the largest difference obtained or the temperature step.

References

- [1] L. Bennett, B. Melchers, and B. Proppe. Curta: A general-purpose high-performance computer at zedat, freie universität berlin. <https://dx.doi.org/10.17169/refubium-26754>, 2020. Accessed July 2025.
- [2] John Carlos Baez. Kosterlitz–thouless transition. Blog post on Azimuth (WordPress), October 2016. Accessed via <https://johncarlosbaez.wordpress.com/2016/10/07/kosterlitz-thouless-transition/>.
- [3] J. M. Kosterlitz and D. J. Thouless. Ordering, metastability and phase transitions in two-dimensional systems. *Journal of Physics C: Solid State Physics*, 6(7):1181–1203, 1973.
- [4] V. L. Berezinskii. Destruction of long-range order in one-dimensional and two-dimensional systems having a continuous symmetry group. i. classical systems. *Soviet Physics JETP*, 32(3):493–500, 1971. Translated from Zh. Eksp. Teor. Fiz. **59**, 907–920 (1970).
- [5] David R. Nelson and J. M. Kosterlitz. Universal Jump in the Superfluid Density of Two-Dimensional Superfluids. *Physical Review Letters*, 39(19):1201–1205, November 1977. Publisher: American Physical Society.
- [6] Glittum and F. Syljuasen. Arc-shaped structure factor in the classical Heisenberg model on the triangular lattice | Phys. Rev. B.
- [7] Cecilie Glittum. Nematic bond theory of frustrated heisenberg models on triangular and honeycomb lattices. Master’s thesis, University of Oslo, Department of Physics, Oslo, Norway, May 2020. Submitted for the degree of Master of Science.
- [8] Han Yan and Johannes Reuther. Low-energy structure of spiral spin liquids. *Physical Review Research*, 4(2):023175, June 2022. Publisher: American Physical Society.
- [9] Matías G. González, Anna Fancelli, Han Yan, and Johannes Reuther. Magnetic properties of the spiral spin liquid and surrounding phases in the square-lattice xy model. *Physical Review B*, 110(8):085106, August 2024.
- [10] Yutaka Okabe and Hiromi Otsuka. Bkt transitions of the xy and six-state clock models on the various two-dimensional lattices. arXiv preprint, January 2025. Version v1 posted 13 January 2025.